The Astrophysical Journal, 735:127 (28pp), 2011 July 10 doi:10.1088/0004-637X/735/2/127

DISCOVERY AND ANALYSIS OF 21 μm FEATURE SOURCES IN THE MAGELLANIC CLOUDS

Kevin Volk[1], Bruce J. Hrivnak[2], Mikako Matsuura[3,15], Jeronimo Bernard-Salas[4], Ryszard Szczerba[5], G. C. Sloan[6], Kathleen E. Kraemer[7], Jacco Th. van Loon[8], F. Kemper[9,16], Paul M. Woods[9,17], Albert A. Zijlstra[9], Raghvendra Sahai[10], Margaret Meixner[1], Karl D. Gordon[1], Robert A. Gruendl[11], Alexander G. G. M. Tielens[12], Remy Indebetouw[13,18], and Massimo Marengo[14,19]

[1] Space Telescope Science Institute, 3700 San Martin Drive, Baltimore, MD 21218, USA; volk@stsci.edu
[2] Department of Physics and Astronomy, Valparaiso University, Valparaiso, IN 46383, USA
[3] Department of Physics and Astronomy, UCL-Institute of Origins, University College London, Gower Street, London WC1E 6BT, UK
[4] Institut d Astrophysique Spatiale, CNRS/Universite Paris-Sud 11, 91405, Orsay, France
[5] N. Copernicus Astronomical Center, Rabianska 8, 87-100 Torun, Poland
[6] Department of Astronomy, Cornell University, Ithaca, NY 14853, USA
[7] Air Force Research Laboratory, AFRL/RVBYB, 29 Randolph Road, Hanscom AFB, MA 01731, USA
[8] Astrophysics Group, Lennard-Jones Laboratories, Keele University, Staffordshire ST5 5BG, UK
[9] Jodrell Bank Centre for Astrophysics, Alan Turing Building, School of Physics and Astronomy, The University of Manchester, Oxford Road, Manchester M13 9PL, UK
[10] Jet Propulsion Laboratory, MS 183-900, California Institute of Technology, Pasadena, CA 91109, USA
[11] Astronomy Department, University of Illinois, 1002 West Green Street, Urbana, IL 61801, USA
[12] Leiden Observatory, P.O. Box 9513, NL-2300 RA Leiden, The Netherlands
[13] Department of Astronomy, University of Virginia, P.O. Box 400325, Charlottesville, VA 22903, USA
[14] Department of Physics and Astronomy, Iowa State University, A313E Zaffarano, Ames, IA 50011, USA
Received 2011 February 7; accepted 2011 April 26; published 2011 June 24

ABSTRACT

Spitzer Space Telescope mid-infrared spectroscopy has been obtained for 15 carbon-rich protoplanetary nebulae (PPNe) in the Large Magellanic Cloud (LMC) and for two other such stars in the Small Magellanic Cloud (SMC). Of these 17 PPNe, the unidentified 21 μm feature is strong in 7 spectra, weak in 2 spectra, and very weak or questionable in 4 spectra. Two of the four spectra without the 21 μm feature have a very strong feature near 11 μm, similar to a feature observed in some carbon-rich planetary nebulae (PNe) in the LMC. We attribute this feature to unusual SiC dust, although the feature-to-continuum ratio is much larger than for SiC features in Galactic or Magellanic Cloud carbon star spectra. The remaining two objects show typical carbon-rich PPNe spectra with no 21 μm features. One of the LMC objects that lacks the 21 μm feature and one SMC object with a questionable 21 μm detection may have mixed dust chemistries based upon their spectral similarity to Galactic [WC] PNe. The 13 objects that either definitely or may show the 21 μm feature have distinct dust shell properties compared to the Galactic 21 μm objects—the 21 μm features are weaker, the estimated dust temperatures are significantly higher, the unidentified infrared (UIR) bands are stronger, and the UIRs show more structure. Four of the 21 μm objects appear to show normal SiC emission features in their spectra. Many of the PPNe show strong 30 μm features, although this feature carries less of the total mid-infrared emission than is normally the case for the Galactic 21 μm PPNe. The LMC objects are in the LMC halo rather than in the LMC bar. The estimated luminosities of these PPNe vary from 4700 to 12,500 $L_{\odot}$.

Key words: circumstellar matter – galaxies: individual (LMC, SMC) – stars: AGB and post-AGB – stars: evolution

Online-only material: color figures

1. INTRODUCTION

Stars of intermediate initial mass (~0.8 to ~8 $M_{\odot}$) are observed to lose a significant fraction of their "birth mass" and to end their existence as white dwarf stars. The last phase of energy production for these stars, on the asymptotic giant branch (AGB), is thought to be the period in which a large part of the mass loss takes place. The mass loss removes the stellar envelope, and when the envelope mass decreases below ~0.001 $M_{\odot}$ (the exact value being a strong function of the core mass) the star leaves the AGB. The core is then exposed, whereupon the star becomes a hot white dwarf and may illuminate a planetary nebula (PN) if sufficient material from the preceding mass loss is still near enough to be excited by the ultraviolet (UV) radiation from the hot core. During the AGB phase the stars dredge up carbon and *s*-process elements due to the interactions between hydrogen and helium shell nuclear reactions. Some fraction of the AGB stars become carbon stars (with C/O > 1) due to this dredge-up of nuclear-processed material. An overview of the properties and evolution of AGB stars is given in Le Bertre et al. (1999).

It is generally thought that the AGB mass loss peaks strongly at the very end of the AGB phase, where the oxygen-rich objects become OH/IR stars and the carbon-rich objects become "extreme carbon stars." In both cases the stars are surrounded by very optically thick dust shells and are optically invisible.

[15] Also at UCL-Institute of Origins, Mullard Space Science Laboratory, University College London, Holmbury St. Mary, Dorking, Surrey RH5 6NT, UK.
[16] Also at Academia Sinica Institute for Astronomy and Astrophysics, P.O. Box 23-141, Taipei 10647, Taiwan.
[17] Also at Department of Physics and Astronomy, University College London, Gower Street, London WC1E 6BT, UK.
[18] Also at National Radio Astronomy Observatory, 520 Edgemont Road, Charlottesville, VA 22903, USA.
[19] Also at Harvard-Smithsonian Center for Astrophysics, 60 Garden St., Cambridge, MA 02138, USA.

For carbon stars the prototypes of the extreme carbon stars are objects such as IRC+10°216 and AFGL 3068. When the star leaves the AGB and the core begins to be exposed, the remnant dust shell can be readily observed during the brief transition phase in which the star has an intermediate temperature compared to AGB stars and PN central stars. These "protoplanetary nebulae" (PPNe) are best identified by their infrared properties, after which optical spectroscopy can be carried out to verify the nature of the objects. Carbon-rich PPNe are expected to have *s*-process element enhancements and show other evidence of the AGB dredge-up. Oxygen-rich PPNe may not have experienced significant dredge-up and so are difficult to identify. PPNe are a subset of the general class of post-AGB objects, which also includes PNe and other objects such as RV Tau stars and possibly R CrB stars (see, e.g., Kwok 1993; Clayton 1996; Szczerba & Górny 2001; Szczerba et al. 2007).

A number of Galactic PPN candidates were identified from the *Infrared Astronomical Satellite* (*IRAS*) all-sky survey (Neugebauer et al. 1984). Four of these objects showed a previously unknown feature at about 21 μm, and other unusual features in their *IRAS* Low Resolution Spectrometer (LRS) data (see Kwok et al. 1989); subsequent optical spectroscopy showed that these stars are carbon-rich PPNe (van Winckel 2003), with lower than solar metallicities. The 21 μm feature carrier has not been identified, although several suggestions have been discussed in the literature (see the review by Posch et al. 2004). The feature is identified unambiguously in a total of only 15 objects in the Galaxy (listed in Hrivnak et al. 2008). The feature has not been positively identified in the spectra of any normal carbon star or in any carbon-rich PN. There has been some suggestion in the literature of a few PNe or AGB stars with extremely weak 21 μm features (see Volk et al. 2000; Hony et al. 2001; Pei & Volk 2003), but in all cases the features are so weak as to be questionable. Most of the other, somewhat unusual mid-infrared features seen in the *IRAS* and later *Infrared Space Observatory* (*ISO*; Kessler et al. 2003) spectroscopy of these objects appear to be a variety of the unidentified infrared (UIR) bands which are commonly seen in carbon-rich PPNe and PNe as well as in the interstellar medium (ISM). These bands are generally accepted to be due to polycyclic aromatic hydrocarbons (PAHs; see the review by Tielens 2008 and references therein). With the greater wavelength coverage of the *ISO* observations it was shown that the 21 μm feature is always accompanied by the broad 30 μm feature, which is commonly observed in the spectra of carbon stars and which is generally attributed to MgS (Hony et al. 2002).

Although a number of the Galactic 21 μm objects are relatively bright at optical wavelengths, none of them has an accurate distance measurement. A few of the stars have *V* magnitudes of about 8 but still do not have an accurate parallax measurement from *Hipparcos* or elsewhere. As a result of this the fundamental properties of the stars are poorly known. Where optical spectroscopy is available, the stars are generally of F-type or G-type, with the hottest of them being of late B-type. Cooler objects of K-type or hotter objects of early B-type and O-type are not found in the sample, and a recent mid-infrared spectroscopic survey of hotter Galactic PPN candidates did not detect any 21 μm objects (Cerrigone et al. 2009).

In this paper, we present observations of new 21 μm objects and a few other carbon-rich PPNe discovered in the Large Magellanic Cloud (LMC) and the Small Magellanic Cloud (SMC) from *Spitzer Space Telescope* spectroscopy. The spectra were taken in a number of programs with varying selection criteria. This introduces unknown selection biases into the original sample, but our selection of carbon-rich PPNe is entirely based on their spectroscopic characteristics so it provides as good a sample as we can get at this time. One bias that can be identified in the sample is that these objects are brighter than average for all objects of similar mid-infrared colors. The LMC objects with spectra discussed in this paper are in the top 33% of IRAC [8.0] and MIPS [24] brightness compared to other objects of similar colors. The SMC objects are in the top 20% of IRAC [8.0] and MIPS [24] brightness compared to other objects with similar colors.

2. CANDIDATE SELECTION

The carbon-rich PPN candidates were selected from the available *Spitzer* Infrared Spectrometer (IRS; Werner et al. 2004; Houck et al. 2004) spectroscopy of targets in the Magellanic Clouds. Objects were considered to be carbon-rich PPNe if they showed the following properties.

1. Typical features due to dust observed in carbon-rich objects and/or carbon-based aromatic molecules (any of the SiC 11 μm, 21 μm, or 30 μm dust features; the UIR features at 6.3, 7.7, 8.6, and 11.2 μm, and possibly the plateau feature observed from 11 to 19 μm).
2. A lower color temperature dust continuum rising from 5 μm and peaking somewhere in the 10–30 μm range (in λF_λ units) indicating the presence of only cool dust, so as to exclude normal carbon stars from the sample.
3. No sign of atomic emission lines, or of the 10 or 18 μm silicate dust features, or of ice absorption bands, or of a continuum rising to peak beyond 40 μm; all so as to exclude young massive stars (whose mid-infrared spectra often show UIR emission) as well as PNe.
4. No strong C_2H_2 or HCN molecular bands if there is no UIR emission, to exclude very dusty extreme carbon stars, although if only the C_2H_2 fundamental band at 13.7 μm were present that would not be grounds for exclusion.
5. Some evidence of an optical counterpart or an excess in the near-infrared, to exclude the extreme carbon stars, although these objects do not generally show the UIR features in their spectra and so can normally be distinguished from the PPNe on that basis.

The last criterion is a secondary requirement because some of the Galactic 21 μm objects have very faint optical counterparts and so similar objects in the Magellanic Clouds might have no detected optical counterpart. They would still be expected to have at least a *K*-band excess compared to the extreme carbon stars which are observed in the LMC and SMC. Conditions (4) and (5) are intended to exclude dusty carbon stars from the candidate sample. There is one known PN in the LMC that would be excluded from the sample by criterion (4), SMP LMC 11 (Bernard-Salas et al. 2006), so it is possible that a similar, but less evolved, carbon-rich post-AGB object with a very high optical depth dust shell would be excluded by mistake. *Midcourse Space Experiment* (*MSX*) SMC 029, which is also excluded by these criteria, may be such an object (Kraemer et al. 2006).

These criteria exclude R CrB stars, which normally do not show the UIR features or any carbon-based dust features and which have continua that rise to a peak in the near-infrared near 2 μm. There are several competing models for the formation of R CrB stars, one of which is that they are carbon-rich post-AGB stars that have experienced a late thermal pulse (see the review

Table 1
Positions and *Spitzer* Observation IDs of the Magellanic Cloud Carbon-rich PPNe

Object	Short Name	α (J2000)	δ (J2000)	AOR	Program ID
SAGE J004441.04−732136.44	J004441	$00^h44^m41\overset{s}{.}04$	$-73°21'36\overset{''}{.}44$	27525120	50240
SAGE J010546.40−714705.27	J010546	$01^h05^m46\overset{s}{.}40$	$-71°47'05\overset{''}{.}27$	27518464	50240
SAGE J050603.66−690355.9	J050603	$05^h06^m03\overset{s}{.}66$	$-69°03'55\overset{''}{.}9$	19006720	30788
SAGE J050713.90−674846.7	J050713	$05^h07^m13\overset{s}{.}90$	$-67°48'46\overset{''}{.}7$	24317184	40159
SAGE J050835.91−711730.6	J050835	$05^h08^m35\overset{s}{.}91$	$-71°17'30\overset{''}{.}6$	25992448	50338
SAGE J051110.64−661253.7	J051110	$05^h11^m10\overset{s}{.}64$	$-66°12'53\overset{''}{.}7$	25992704	50388
SAGE J051228.18−690755.8	J051228	$05^h12^m28\overset{s}{.}18$	$-69°07'55\overset{''}{.}8$	24316928	40159
SAGE J051828.18−680404.0	J051828	$05^h18^m28\overset{s}{.}18$	$-68°04'04\overset{''}{.}0$	19011840	30788
SAGE J051845.23−700534.5	J051845	$05^h18^m45\overset{s}{.}23$	$-70°05'34\overset{''}{.}5$	24314624	40159
SAGE J052043.86−692341.0	J052043	$05^h20^m43\overset{s}{.}86$	$-69°23'41\overset{''}{.}0$	27985920	50338
SAGE J052520.76−705007.5	J052520	$05^h25^m20\overset{s}{.}76$	$-70°50'07\overset{''}{.}5$	25996032	50338
SAGE J052902.39−661527.7	J052902	$05^h29^m02\overset{s}{.}39$	$-66°15'27\overset{''}{.}7$	11239680	03591
SAGE J053525.86−711956.6	J053525	$05^h35^m25\overset{s}{.}86$	$-71°19'56\overset{''}{.}6$	19008256	30788
SAGE J053632.56−701738.4	J053632	$05^h36^m32\overset{s}{.}56$	$-70°17'38\overset{''}{.}4$	24315648	40159
SAGE J055311.98−701522.7	J055311	$05^h53^m11\overset{s}{.}98$	$-70°15'22\overset{''}{.}7$	27084032	40159
SAGE J055825.96−694425.8	J055825	$05^h58^m25\overset{s}{.}86$	$-69°44'25\overset{''}{.}8$	25992960	50338
IRAS F06111−7023	F06111	$06^h10^m32\overset{s}{.}02$	$-70°24'40\overset{''}{.}8$	19013120	30788

Note. The positions are from the SAGE LMC and SMC surveys for all the sources except for IRAS F06111−7023, for which the 2MASS catalog position is used due to the relatively low accuracy of the *IRAS* position.

Clayton 1996). They do not appear to be the progenitors of typical PNe. There are a very few hot (∼20,000 K) R CrB stars that show UIR emission and have otherwise featureless mid-infrared spectra, so there is a possibility that such objects might be included in the sample if the dust continuum temperature were low. One of these hot R CrB stars, HV 2671 (Clayton et al. 2007), is in the LMC and has an IRS spectrum. It was not included as a PPN candidate because the continuum rises to the short-wavelength end of the IRS spectral range, violating requirement (2) above.

These selection criteria are entirely independent of the general classification scheme for the *Spitzer* IRS spectra of LMC objects proposed in Woods et al. (2011). That scheme would classify any of the sample objects that have an obvious 21 μm feature or a double-peaked spectral energy distribution (SED) as being carbon-rich post-AGB stars, which is consistent with conditions (1) and (5) above. However, that scheme does not recognize objects with strong UIRs and the 30 μm feature as candidate carbon-rich post-AGB objects solely on this basis. The classification flow chart (Figure 2 in Woods et al. 2011) requires one of (1) strong SiC 11.3 μm and 30 μm dust features or (2) a double-peaked SED, or (3) a 21 μm feature to assign a spectrum with carbon-star-type dust features as being a carbon-rich post-AGB star, and makes no mention of the UIR features. For this paper, we assume that objects with extremely strong UIRs are likely carbon-rich post-AGB stars if they pass the other criteria listed above. Objects with strong UIR features, but no atomic emission lines and no other silicate- or carbon-based dust features, are classified as being "evolved young stellar objects" (YSOs) in the Woods et al. (2011) scheme. This produces a misclassification of PPNe and PNe which have strong UIR features, no emission lines, and which lack the SiC, 21 and 30 μm features. Such objects are rare in the Galaxy, and generally appear to be sources of mixed dust shell chemistry (see Section 4.1). The two objects in our sample that appear to have unusual SiC emission features (as will be discussed in Section 3.4) would be either classified as carbon-rich AGB stars or as "other" in the Woods et al. (2011) scheme.

All publicly available spectra of LMC objects in the *Spitzer* archive were examined, as part of the SAGE-Spec project (Kemper et al. 2010). Preliminary by-eye classifications of all the LMC spectra were made by G. Sloan and K. Kraemer as well as independently by K. Volk, from which the PPN candidates were selected. PPN candidates were found from programs 40159 (PI: A. Tielens), 3591 (PI: F. Kemper), 50338 (PI: M. Matsuura), 30788 (PI: R. Sahai) and the GTO program 50240 (PI: G. Sloan). The Matsuura sample is discussed in M. Matsuura et al. (2011, in preparation).

The carbon-rich PPNe that we have found were originally selected for IRS observation based primarily on their mid-infrared colors. The objects for R. Sahai's program were selected as having large *IRAS* [25]/[12] flux ratios, for which they were likely to be either carbon stars with thick dust shells or PPNe. The other objects were chosen from the SAGE (Meixner et al. 2006) or SAGE-SMC (Gordon et al. 2010) catalogs as either having low color temperatures or showing evidence of having a double-peaked SED, which is commonly the case for PPNe.

The 17 objects thus selected, along with their positions, are listed in Table 1. For all those objects identified in the SAGE LMC or SMC surveys the position is taken from these catalogs using the Infrared Array Camera (IRAC; Fazio et al. 2004) position. For the one object outside the SAGE survey area, IRAS F06111−7023, the Two Micron All Sky Survey (2MASS; Skrutskie et al. 2006) position of the counterpart is given as the source position. This 2MASS position is about 2″ from the *MSX* (Mill et al. 1994) position for the source and is also slightly different than the position of the *Spitzer* IRS observation, but there is no other 2MASS source in the vicinity that could plausibly be the counterpart of the mid-infrared source.

The IRS spectra of four objects in the sample (J050713, J051228, J051845, and J052902) were presented in Figure 7 of Kemper et al. (2010). Only J051845 has an immediately obvious 21 μm feature. The feature is very weak in J050713, absent in J051228, and weak in J052902. In this paper, the sample of objects considered is about four times larger than in the SAGE-Spec overview paper.

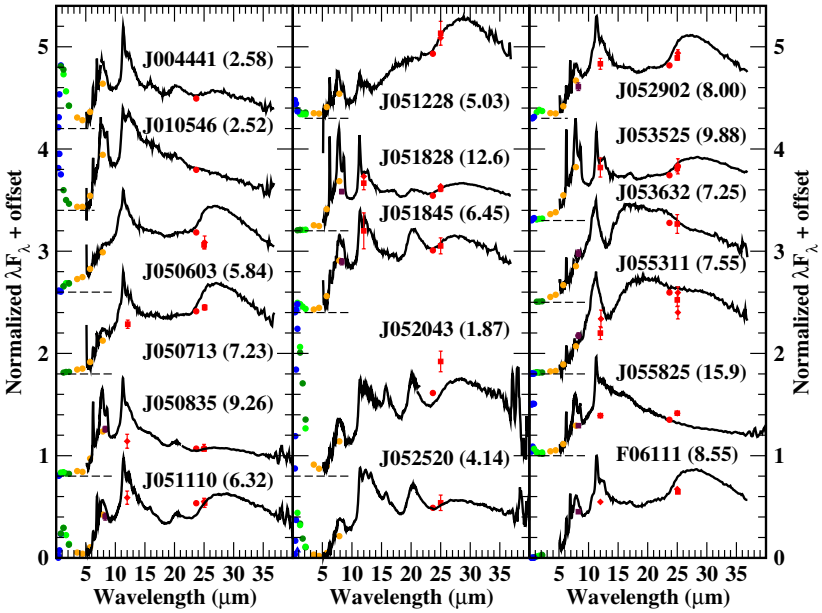

Figure 1. *Spitzer* IRS spectra (black lines) of the carbon-rich PPNe in the Magellanic Clouds. Each spectrum is normalized to 1.0 at the peak of the mid-infrared emission, and the spectra are offset vertically. The short-dashed lines on the left in each panel indicate the offset zero levels. Also plotted for each object are the available photometry points. They are in color in the online version: *Spitzer* IRAC (orange), *Spitzer* MIPS [24] (red circles), *IRAS* point source catalog (red squares), *IRAS* faint source catalog (red diamonds), 2MASS (green), DENIS (dark green), *MSX* (maroon), and MCPS (blue). The various data sets for a particular object have not been scaled relative to one another. The peak λF_λ values in units of 10^{-14} W m^{-2} are listed to the right of the object name for the different objects. The IRS spectra of J050835, J05110, J052043, J052520, and J055825 have been smoothed over five points to reduce the noise.

(A color version of this figure is available in the online journal.)

3. *SPITZER* IRS OBSERVATIONS

3.1. Data Reduction

The Matsuura program observations (objects J050835, J051110, J052043, and J052520) were processed by J. Bernard-Salas using the Spitzer Science Center's pipeline (version 18.7) which is maintained at Cornell and using the "Smart" reduction package (Higdon et al. 2004; Lebouteiller et al. 2010). The basic calibrated data were used. The reduction began by removing and replacing unstable sensitive pixels (rogue pixels) using the Spitzer Science Center tool "irsclean." The next step consisted of averaging the individual exposures for each IRS module. Fringes were present in the Long Low 1 module (20–24 μm) in some objects and were removed using the defringe tool in Smart. Checks were made to ensure that the defringing did not change the continuum shape of the spectra. All the targets were observed with the high-resolution modules, and the spectra were extracted using full aperture extraction. The spectral orders were then combined into the final spectra.

The remaining LMC spectra are from the SAGE-Spec sample. Details of the reduction and calibration are given by Kemper et al. (2010). The SMC spectra from GTO program 50240 were reduced using the same procedure as for the LMC SAGE-Spec data.

3.2. The Spectra

Figure 1 presents the IRS spectra of the 17 objects along with the available photometry from the *Spitzer* IRAC and Multiband Imaging Photometer for *Spitzer* (MIPS; Rieke et al. 2004) instruments, *MSX* (Egan et al. 2003), *IRAS* (Beichman et al. 1988), 2MASS, the Deep Near-Infrared Survey (DENIS; Fouqué et al. 2000), and the Magellanic Clouds Photometric Survey (MCPS; Zaritsky et al. 1997). The cross-identifications in these catalogs as well as in the United States Naval Observatory B (USNO-B; Monet et al. 2003) and Guide Star Catalog 2.3.2 (GSC-2; Lasker et al. 2008) catalogs are listed in Table 2.

Of the 17 objects, the 21 μm feature is strong in seven objects (J004441, J050835, J051110, J051828, J051845, J052043, and J052520), weak but still easily visible in two objects (J050713 and J052902), and of questionable shape or very weak in four other objects (J010546, J050603, J053525, and F06111). J010546 has structure in the spectrum near 20 μm which may be the 21 μm feature, or it may be some other feature(s), or just be due to noise, which makes the identification questionable. The remaining four objects (J051228, J053632, J055311, and J055825) do not appear to have the 21 μm feature. The IRS spectrum of J051228 is noisy around 20 μm but the general continuum shape interpolated from the adjacent wavelengths is consistent with there being a smooth, featureless continuum from 14 to 23 μm.

Two objects with unusual spectra which may or may not be carbon-rich PPNe, J053632 and J055311, are included in this sample (see Figure 1). These two spectra show weak UIR features and have no silicate features. The continuum rises to a peak at 15–20 μm which suggests that the dust shell contains only cool dust, typical for PPNe spectra. Both spectra show a strong feature near 11 μm which *may* be the SiC feature. These features are very similar to features observed in a handful of carbon-rich PNe in the LMC (Bernard-Salas et al. 2009) which was attributed to SiC. This feature will be discussed further in Section 3.4. J055311 appears to have a weak 30 μm feature while J053632 has features on the spectrum at 23 and 31 μm which we cannot identify.

Figure 2 shows the IRS spectra of the 15 "normal" carbon-rich PPNe from 15 to 25 μm to highlight the 21 μm feature (which peaks at 20.1 μm; see Volk et al. 1999). The lines drawn at 18.8, 20.1, and 23 μm show the approximate short-wavelength edge of the feature, the peak wavelength, and the approximate

Table 2
Designations for the Magellanic Cloud Carbon-rich PPNe

SAGE Name	2MASS Name	DENIS Name	*MSX* Name	*IRAS* Name	USNO Name	GSC-2 Name	Other Names
J004441.04−732136.44	J00444111−7321361	J004441.1−732136 J004441.1−732135	···	···	0166-0023129	S010202254947	S3MC J004441.03−732136.09
J010546.40−714705.27	J01054645−7147053	J010546.3−714705 J010546.4−714705	···	···	0182-0026616[a]	S010202073539[a]	···
J050603.66−690355.9	J05060367−69035587	J050603.7−690356	G280.0584−34.5413	05063−6908	···	···	···
J050713.90−674846.7	J05071393−67484867	No detection[b]	···	05073−6752	···	···	
J050835.91−711730.6	J05083592−71173006	J050835.9−711731 J050835.9−711730	G282.5914−33.7610	05092−7121	0187-0063281	S010101335622	···
J051110.64−661253.7	J05111065-6612537	J051110.6−661253 J051110.5−661253	G276.5492−34.7037[c]	05110−6616	0237-0048433	S01120201170	···
J051228.18−690755.8	J05122821−6907556	J051228.2−690756	···	05127−6911 Z05127−6911[d]	0208-0081614	S01320337781	···
J051828.18−680404.0	J05182817−6804040	J051828.0−680403	G278.5836−33.6534	05185−6806 F05186−6807	No detection[e]		LI-LMC0777
J051845.23−700534.5	J05184525−7005344	J051845.3−700534	G280.9567−33.2286	F05192−7008	0199-0091349	S013202126097	···
J052043.86−692341.0	J05204385−6923403	J052043.8−692340 J052043.7−692341	···	S05211−6926[f]	0206-0093670	S013203139249	···
J052520.76−705007.5	J05252077−7050075	J052520.8−705007	···	Z05259−7052[d]	0191-0075020	S010103215795	···
J052902.39−661527.7	J05290241−6615277	···	G276.2542−32.9195[c]	F05289−6617	···	···	NGC 1978 WBT 2665[g] NGC 1978-IR3
J053525.86−711956.6	J05352583−7119566	J053526.0−711957	···	F05361−7121	···	···	···
J053632.56−701738.4	J05363246−7017375	J053632.4−701737	G280.8852−31.7098	05370−7019	0197-0161431[h]	···	···
J055311.98−701522.7	J05531196−7015226	J055311.9−701523 J055311.9−701522	G280.6756−30.3174	05537−7015	0197-0161431[i]	S01010021932[i]	···
J055825.96−694425.8	J05582596−6944257	J055825.9−694425 J055826.0−694426	G280.0531−29.8947	05588−6944 F05588−6944	0202-0152879	S010100253989	···
No detection[j]	J06103202−7024408	J061032.0−702440	G280.8021−28.8524	F06111−7023	···	···	···

Notes. For a number of objects the DENIS survey detected the object at slightly different positions in the two epochs leading to two entries for the same object. Where this is the case, both names are listed. For *IRAS* sources two names are given if the source is listed in more than one catalog with different names.

[a] The USNO/GSC measurements may include two other stars close by to the northwest.

[b] The closest DENIS sources J050712.4−674846 and J050712.3−674847 are not the PPN.

[c] This is an *MSX* point source reject.

[d] This is an *IRAS* Faint Source Catalog point source reject.

[e] There is a very faint candidate optical counterpart at the position and a star of $V \sim 21$ visible $2''$ to the northwest.

[f] This is an IRAS Serendipitous Source Catalogue name. The positional discrepancy between the *IRAS* and SAGE positions is larger than usual, but the PPN is the only MIPS [24] source in the vicinity.

[g] A brighter star $\sim 3''$ to the southeast is not the optical counterpart.

[h] This association is doubtful due to an $\sim 1\farcs5$ position discrepancy.

[i] The optical counterpart is offset $\sim 1''$ from the infrared position so the association is tentative.

[j] This object is outside the SAGE survey area. The 2MASS position is used for cross-identification.

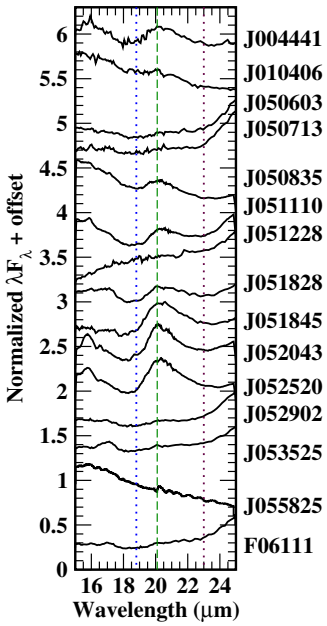

Figure 2. IRS spectra for the 15 objects with typical carbon-rich PPNe spectra are replotted here from 15 to 25 μm, normalized to 1 at 20 μm and offset to separate the different objects. The dashed line marks the 21 μm feature peak wavelength. The two dotted lines show the approximate starting and ending wavelengths of the feature. As can be seen in this figure, there is some variation in the positions of the spectral minima at shorter and longer wavelengths around the feature, likely due to variations in the continuum shape and in the strength of the adjacent features.

(A color version of this figure is available in the online journal.)

long-wavelength edge of the feature, respectively. In searching for the presence of the 21 μm feature we looked for inflections on the continuum around the "edge" wavelengths and for an inflection at the peak wavelength. The positions of the inflections at shorter and longer wavelengths appear to vary somewhat depending on the strengths of the UIR plateau and the 30 μm feature.

Figure 3 shows the short-wavelength region of Figure 1, where most of the UIR features are located. The normal UIR features are at 3.3, 6.3, 7.7, 8.6, and 11.2 μm. Some Galactic objects with very strong UIR emission, such as HD 44179 (the Red Rectangle), are observed to have additional weaker features which are assumed to be other UIR emission modes (Tielens 2008). Most of the Galactic 21 μm objects have unusual UIR properties compared to the Red Rectangle and most other objects showing the UIR features, as will be discussed in Section 4. The LMC and SMC objects show more "normal" looking UIR features, as a rule.

A summary of the features observed in the different spectra is listed in Table 3. Features listed include dust features (11 μm SiC, 21 μm, and 30 μm), the main UIR features (6.3, 7.6/7.8, 8.6, and 11.2 μm), the weaker UIR features thought to be from PAHs or other carbon-based molecules (6.9, 7.25, 12.0, 12.4, 12.6, 12.8, and 13.3 μm), and finally the 15.8 μm feature (Hrivnak et al. 2009). In addition the estimated end wavelength of the plateau under the 11.2 feature is listed in the table. This was taken to be the wavelength where the continuum reaches a local minimum and turns up.

3.3. Comments on Individual Objects

This section presents comments on the photometry of the different objects at shorter wavelengths and any known associations, and some general notes about the infrared spectra. All of the LMC objects in the sample are bright enough in the mid-infrared that they were first discovered by the *IRAS* mission, although many of them were only detected in the [25] filter near the *IRAS* sensitivity limit, which made determination of their nature impossible. Given the relative sensitivities of the *IRAS* bands, objects only detected at [25] must have a relatively low (<300 K) infrared color temperature. There are some limits on how low a color temperature such sources can have without being detected at longer wavelengths, but this places only loose constraints on the nature of the objects. The two SMC objects have observed brightnesses in the 10–20 μm wavelength range

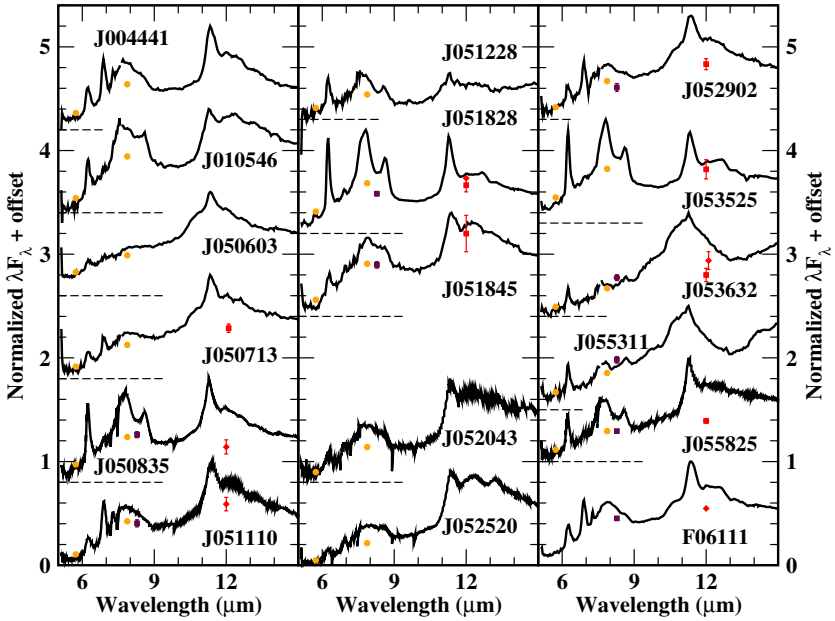

Figure 3. Same as Figure 1 but with the *x*-axis range adjusted to show the shorter wavelength UIR features more clearly. The *y*-axis scalings of the data for the individual objects have not been changed from Figure 1.

(A color version of this figure is available in the online journal.)

Table 3
Features Observed in the Magellanic Cloud Carbon-rich PPN Spectra

Object	6.3	6.9	7.25	7.7	8.6	11.2	12.0	12.4	12.6	12.8	13.3	15.8	λ_{long}[a] (μm)	11	21	30
J004441	W	S	Y	B	B	Y	Y	Y	N	N	N	Y	18.0	N	Y	Y
J010546	Y	N	N	Y	Y	Y	N	Y	N	N	Y	N	18.2	N	W?	W?
J050603	Y	vW	N	B	B	Y	N	N	N	Y	N	N	18.4	Y	vW	S
J050713	Y	Y	N	B	B	Y	Y	N	Y	N	N	N	18.1	Y	W	S
J050835	Y	Y	N	Y	Y	Y	Y	N	N	N	N	N	18.0	N	Y	Y
J051110	Y	S	Y	mB	mB	Y	N	Y	N	N	N	N	18.4	N	Y	W
J051228	Y	Y	vW	Y	Y	Y	N	Y	N	N	N	N	13.4	N	N	Y
J051828	Y	W	N	Y	Y	Y	Y	Y	N	Y	N	Y	18.2	N	Y	S[b]
J051845	Y	W	N	mB	mB	Y	N	N	N	N	N	W?	17.8	N	Y	Y
J052043	Y	Y	N	B	B	Y	N	N	N	N	Y	S	18.0	N	Y	Y
J052520	Y	Y	N	B	B	Y	N	N	N	N	Y	Y	18.2	N	Y	W
J052902	Y	Y	W	mB	mB	Y	N	N	N	N	N	W	18.2	Y	W	S
J053525	Y	vW	N	Y	Y	Y	N	N	N	N	N	N	18.4	N	vW	S
J053632	Y	N	N	Y	Y	Y	N	N	N	N	N	N	...	Y[c]	N	N
J055311	Y	N	N	Y	Y	Y	N	N	N	N	N	N	...	Y[c]	N	N
J055825	Y	vW	N	Y	Y	Y	N	N	N	N	N	W?	19.7	N	N	W
IRAS F06111	Y	S	Y	mB	mB	Y	N	N	Y	N	N	W	18.2	Y	vW	Y

Notes. The table entries are: Y for "yes," N for "no," S for "strong," W for "weak," vW for "very weak." In cases where the feature may be present but is marginal the entry "W?" is used. When the 7.7 and 8.6 UIR features are not resolved as separate features, these columns have the entry B for "blend." When the 8.6 μm feature can be seen on the combined profile, but it is very weak, both the 7.7 and 8.6 μm features are labeled mB for "marginal blend."
[a] The long-wavelength end of the plateau feature that starts at about 11 μm. While this plateau is not usually observed in the interstellar medium, it is observed in Galactic PPNe and in some Galactic PNe.
[b] The peak wavelength is shifted $\sim$2 μm to longer wavelengths.
[c] The feature is unusual.

that are $\sim$4 times fainter than is the case for the LMC objects, and so neither of them was detected by *IRAS* as they were below its detection threshold. With a correction for the relative distances of the LMC and SMC, this means that the mid-infrared emission at these wavelengths is roughly three times smaller in absolute terms for the SMC objects than for the LMC objects.

The photometry for these objects from the literature is presented in Table 4, along with the uncertainties.

SAGE J004441.04−732136.44. The optical counterpart is relatively bright (the MCPS *V* magnitude is 15.96) and is detected in the GCS-2 and USNO-B catalogs. It was also detected by 2MASS and DENIS. There were no pre-*Spitzer* mid-infrared detections of this source so we have very little information about possible variability of the dust emission.

SAGE J010546.40−714705.27. The IRS spectrum shows strong UIR features similar to those of the Galactic carbon-rich PN IRAS 21282+5050 (Beintema et al. 1996), along with the weak and noisy bump near 20 μm which we tentatively identify as a 21 μm feature. At longer wavelengths the spectrum shows a slight curvature in the continuum which possibly indicates a very weak 30 μm feature. There is no MIPS [70] detection of this object to help define the long-wavelength continuum shape. Most Galactic objects with spectra similar to this source have mixed circumstellar chemistries (see Section 4.1), but in this case there are no crystalline silicate features detected in the 24–30 μm region of the spectrum so it is not clear whether this is an object of mixed chemistry.

As with J004441 there were no pre-*Spitzer* mid-infrared observations of this object. There is a relatively bright MCPS optical counterpart very close to the SAGE position with $V = 15.44$, which does not appear to have been the subject of any previous publications. The DENIS I_c magnitude measurements for the object are slightly different than the MCPS I_c photometry (15.09 for the MCPS and 15.00/14.88 for the DENIS observations) which may indicate a low level of optical/near-infrared variability given that the stated uncertainties in these individual magnitudes are a few times smaller than the differences between the values.

SAGE J050603.66−690355.9. The UIR features in this spectrum are rather weak. The large feature near 11 μm is attributed to SiC as is discussed in Section 3.4.

There is no convincing optical counterpart for this source. The nearest MCPS source is 2.″8 away and its colors are not what would be expected for a source of this type. There is also no candidate counterpart at the source position in the Digitized Sky Survey images (Djorgovski et al. 1999).

In the literature IRAS 05063−6908 was tentatively identified as the infrared counterpart of the PN LMC SMP 025 by Leisy et al. (1997). This turns out to be an incorrect association, as LMC SMP 025 is 1.′9 from J050603.

SAGE J050713.90−674846.7. The mid-infrared spectrum of the object is similar to that of J050603. The UIR features are somewhat stronger here than in the case of J050603, and again an SiC feature is suspected around 11 μm.

There is no detection of this object at wavelengths shorter than the *J* band. No optical counterpart with $V < 21.5$ or $I_c < 20.5$ is detected in the MCPS with a radius of 3″, and there is no evidence of an optical counterpart in the Digitized Sky Survey images. The *IRAS* source is listed as TRM 009 in Reid et al. (1990), and several possible optical counterparts are given in Table 2 of their paper. None of these turn out to be correct; the closest one is 11″ from the *Spitzer* position.

SAGE J050835.91−711730.6. The IRS spectrum of this LMC object is more similar to that of the SMC object J004441 than it is to the spectra of any of the other LMC objects.

The optical counterpart, while definitely detected in the MCPS ($V \sim 18.4$), is relatively faint whereas for J004441 the optical counterpart is significantly brighter. The short-wavelength part of the SED peaks at *J* band, and the optical colors are fairly red. Comparison of the 2MASS and

Table 4
Photometry for the Magellanic Cloud Carbon-rich PPNe

Object	MCPS				DENIS			2MASS			IRAC				MIPS		*IRAS*		*MSX*		
	U	B	V	I_c	I_c	J	K	J	H	K_S	[3.6]	[4.5]	[5.8]	[8.0]	[24]	[70]	[12] (Jy)	[25] (Jy)	[8.28] (Jy)	[12.13] (Jy)	[21.34] (Jy)
J004441	19.248	17.524	15.960	14.457	14.444	13.62	12.941	13.626	13.233	13.021	12.329	11.901	10.388	8.334	5.141	...	...	...	...	...	...
±	0.149	0.024	0.179	0.036	0.04	0.11	0.10	0.042	0.05	0.044	0.035	0.036	0.042	0.033	0.009	...	...	...	...	...	...
J010546	15.435	15.816	15.439	15.093	14.938	14.615	...	14.945	14.598	14.608	13.573	12.873	10.577	8.109	4.899	...	...	...	...	...	...
±	0.032	0.029	0.057	0.032	0.09	0.05	...	0.057	0.104	0.111	0.035	0.040	0.029	0.025	0.008	...	...	...	...	...	...
J050603	...	...	...	...	...	15.17	13.15	15.193	13.899	13.209	11.242	10.354	9.170	7.558	3.569	...	...	0.225	0.090	...	0.906
±	...	...	...	...	...	0.05	0.20	0.085	0.059	0.048	0.040	0.100	0.031	0.021	0.007	...	...	0.018	0.006	...	0.079
J050713	...	...	...	...	...	...	...	16.572	15.317	14.533	12.226	11.326	9.686	7.567	3.258	...	0.141	0.392	...	...	...
±	...	...	...	...	...	...	...	0.056	0.047	0.046	0.016	0.046	0.007	0.011	0.026	...	0.028	0.027	...	...	...
J050835	...	20.178	18.379	16.493	16.27	15.095	...	15.343	14.755	14.156	11.759	11.221	8.948	6.931	3.902	3.049	0.126	0.216	0.117	...	...
±	0.050	0.027	0.084	0.12	0.15	...	0.040	0.028	0.037	0.055	0.099	0.057	0.017	0.050	0.009	0.025	0.024	0.007	...	...	
J051110	20.528	18.416	16.629	14.536	14.504	13.292	12.56	13.295	12.844	12.680	12.130	11.679	9.920	7.382	3.564	3.767	0.149	0.291	0.071	...	...
±	0.192	0.050	0.033	0.024	0.009	0.015	0.11	0.025	0.030	0.029	0.032	0.029	0.026	0.019	0.006	0.073	0.016	0.017	0.006	...	...
J051228	15.598	16.586	16.154	16.129	15.922	15.292	13.777	15.682	14.927	14.175	12.420	11.798	10.106	8.251	3.643	1.172	...	0.375	...	...	...
±	0.067	0.046	0.046	0.052	0.060	0.140	0.320	0.083	0.095	...	0.041	0.033	0.028	0.016	0.006	0.055	...	0.049	...	...	...
J051828	...	...	...	...	18.041	16.301	...	16.692	15.641	14.604	11.353	10.808	8.383	6.491	3.334	1.551	0.234	0.432	0.133	...	...
±	...	...	...	...	0.190	0.230	...	0.050	0.039	0.039	0.023	0.022	0.027	0.021	0.025	0.050	0.033	0.030	0.007	...	...
J051845	20.134	19.207	17.481	15.646	15.653	14.572	13.717	14.656	14.219	13.989	12.763	11.566	9.428	7.190	3.413	1.998	0.206	0.351	0.088	...	...
±	0.158	0.062	0.050	0.093	0.050	0.12	0.21	0.025	0.027	0.030	0.049	0.039	0.035	0.018	0.012	0.047	0.045	0.042	0.006	...	...
J052043	17.618	16.515	15.075	13.887	13.78	13.049	12.42	12.977	12.517	12.385	12.583	12.370	11.310	8.939	4.461	...	...	0.155	...	...	...
±	0.070	0.056	0.075	0.051	0.13	0.011	0.22	0.034	0.044	0.044	0.059	0.042	0.026	0.017	0.038	...	...	0.016	...	...	...
J052520	17.562	16.570	15.335	16.252	14.287	13.667	13.279	13.627	13.445	13.310	13.140	12.976	11.268	8.595	4.119	3.013	...	0.186	...	...	...
±	0.040	0.030	0.020	0.080	0.03	0.09	0.19	0.029	0.033	0.038	0.078	0.042	0.050	0.031	0.009	0.007	...	0.026	...	...	...
J052902	...	22.101	21.408	17.354	...	...	...	14.771	13.617	13.022	11.903	11.211	9.521	7.325	3.328	2.296	0.171	0.395	0.068	...	...
±	...	0.227	0.131	0.049	...	...	...	0.064	0.068	0.043	0.045	0.074	0.018	0.014	0.028	0.027	0.017	0.016	0.056	...	...
J053525	...	...	...	...	...	16.023	13.955	16.437	15.216	14.174	11.437	10.446	8.494	6.669	3.315	1.502	0.205	0.422	...	...	...
±	...	...	...	...	...	0.19	0.35	0.052	0.044	0.034	0.035	0.021	0.019	0.016	0.025	0.034	0.037	0.030	...	...	...
J053632[a]	20.438	21.230	18.783	18.058	18.106	...	...	17.241	16.303	15.215	11.929	10.840	9.205	7.386	2.964	2.477	...	0.567	0.100	...	...
±	0.371	0.244	0.172	0.070	0.19	...	...	0.009	0.13	0.008	0.031	0.028	0.039	0.018	0.023	0.076	...	0.040	0.007	...	...
J055311[b]	20.300	20.144	20.533	19.311	17.67	16.257	...	16.280	15.740	14.945	12.792	11.895	9.900	7.736	2.995	2.253	0.156	0.481	0.075	0.447	...
±	0.188	0.066	0.105	0.466	0.24	0.055	...	0.046	0.060	0.055	0.032	0.027	0.025	0.022	0.006	0.030	0.025	0.024	0.006	0.047	...
J055825	15.979	16.044	15.418	14.918	14.87	14.60	13.17	14.685	14.364	13.754	11.330	10.389	8.829	6.779	3.039	2.161	0.258	0.495	0.129	...	...
±	0.048	0.024	0.022	0.014	0.13	0.035	0.24	0.027	0.028	0.029	0.169	0.190	0.091	0.032	0.008	0.030	0.018	0.020	0.007	...	...
F06111	21.034	20.984	20.445	19.861	18.038	...	13.906	16.320	14.880	14.166	...	...	...	...	...	...	0.184	0.480	0.107	...	...
±	0.266	0.171	0.075	0.423	0.017	...	0.24	0.097	0.082	0.065	...	...	...	...	...	...	0.048	0.019	0.067	...	...

Notes. For each object the photometry values are listed followed by the uncertainties on the second line. Values are given in Jansky for the *IRAS* and *MSX* observations, rounded off to three decimal places in all cases, and in magnitudes for the other observations. The DENIS magnitudes are averaged in those cases where the object position in the catalog differed between the two epochs (see Table 2) and the uncertainties listed are the 1σ values in these instances. For the SAGE observations the epoch 1 and epoch 2 photometry were averaged where both values are available, and the uncertainties are the 1σ values. Otherwise the magnitudes and their uncertainties are given to the original catalog precisions.

[a] The optical and near-infrared counterpart is $\sim 1\farcs5$ away from the SAGE position and may not be the same object.

[b] The faint optical counterpart in the MCPS is $\sim 1''$ from the SAGE position and thus may not be the same object. The available optical and I_c photometry from DENIS and USNO-B are inconsistent with the MCPS V and I_c measurements. By contrast the USNO-B blue photometry appears to be consistent with the MCPS B and U photometry.

DENIS photometry suggests moderate variability of the star ($\Delta J \sim 0.3$).

SAGE J051110.64−661253.7. There is a bright optical counterpart to this object in the MCPS which is also detected in the GSC-2. The photometry suggests intermediate levels of dust obscuration, as the stellar part of the SED peaks around *J* band and then declines significantly between *V* and *U* in the optical. Optical spectroscopy in the red part of the visible yields a spectral type of F3 II(e) for this star (van Aarle et al. 2011). A spectrum at shorter wavelengths from Gemini South Observatory (program GS-2009B-Q-97) shows the very reddened continuum shape but did not allow a spectral type to be determined because the star is too faint at wavelengths below 4500 Å where the classical spectral type indices are found (B. J. Hrivnak et al. 2011, in preparation).

SAGE J051228.18−690755.8. There is a bright optical counterpart to this object which is listed in the MCPS, USNO, and GSC-2 catalogs. The relatively blue $U - B$ and $B - V$ colors of the star and the low-temperature mid-infrared continuum both suggest that the star is relatively hot and is entering the early PN phase. An optical spectrum taken at the Gemini South Observatory (also program GS-2009B-Q-97) shows strong, low excitation nebular emission lines and yields a spectral type of B0.5I(e) (B. J. Hrivnak et al. 2011, in preparation).

The mid-infrared spectrum of this object is very similar to that of IRAS 01005+7910, a Galactic early B-type carbon-rich post-AGB star. While IRAS 01005+7910 is a carbon-rich PPN, both *ISO* observations (Hrivnak et al. 2000) and more recent *Spitzer* IRS data (Cerrigone et al. 2009) conclusively show that it does not have any trace of a 21 μm feature. J051228 also shows no sign of the 21 μm feature and has the 30 μm feature shifted to longer wavelengths compared to most of the other objects in the sample. In contrast to the other sample objects for which the UIR plateau extends to ∼18 μm, for J051228 the plateau extends only to 13.4 μm.

SAGE J051828.18−680404.0. The optical counterpart of the object is faint and is only detected in the I_c filter in the DENIS survey. The IRAC [3.6] and [4.5] photometry suggests that the object may have a strong 3.3 μm feature. This object was identified as a likely post-AGB object by van Loon et al. (1997) and is also known as LI-LMC0777.

J051828 has unusually strong UIR features, which somewhat overshadow the 21 and 30 μm features seen at longer wavelengths.

SAGE J051845.23−700534.5. The MCPS photometry for this object gives colors $V - I_c$ of 1.83, $B - V$ of 1.72, and $U - B$ of 1.07. The large $V - I_c$ value would normally suggest that the star is a carbon star or a late M-type star, but $B - V$ and $U - B$ would be larger than $V - I$ for these spectral types. The odd colors probably indicate a somewhat grayer extinction from the dust shell around the star than is usual from dust in the ISM, implying that the dust grains are larger than normal. If the star is obscured, and we are primarily seeing scattered light from the envelope, that might also help explain the strange color values.

SAGE J052043.86−692341.0. The *IRAS* source SSSC 05211−6926 is only detected at [25], and the *IRAS* position is ∼16″ from the SAGE position. This is a larger positional error than usual for the *IRAS* point sources that correspond to these IRS sources, but the flux is consistent with it being the same object. A search of the SAGE MIPS [24] catalog shows that there is no other plausible MIPS counterpart to the *IRAS* source. The *IRAS* [25] flux measured for source 05211−6926 is ∼30% higher than the MIPS [24] measurement for the source. The nominal uncertainty in the *IRAS* flux measurement is 9%.

This object has the largest optical to infrared flux ratio of any of the objects in our sample, indicating a comparatively low dust optical depth. The optical colors suggest that the star is of intermediate spectral type (F or G). Optical spectroscopy in the red part of the visible yields a spectral type of F5 Ib(e) for this star (van Aarle et al. 2011), while another optical spectrum at shorter wavelengths from Gemini Observatory (also program GS-2009B-Q-97) gives a spectral type of F8I(e) (B. J. Hrivnak et al. 2011, in preparation).

One unusual aspect of the mid-infrared spectrum is that while the 11.2 μm UIR component is present, the contrast between this feature and the underlying plateau is smaller than for many of the other spectra in Figure 1.

SAGE J052520.76−705007.5. There is a bright optical counterpart ($V = 15.3$) detected in the USNO-B, GSC-2, and MCPS catalogs. The SED suggests a moderate dust optical depth from the ratio of optical to infrared emission.

The IRS spectral properties are very similar to those of the Galactic 21 μm object IRAS 06530−0213 (Hrivnak et al. 2009) but the UIR features are ∼3 times stronger for J052520 than for IRAS 06530−0213.

SAGE J052902.39−661527.7. The optical counterpart is detected at $V = 21$ in the MCPS and is also known as cluster star NGC 1978 WBT 2665 (Will et al. 1995). The photometry at short wavelengths indicates a significant dust optical depth since the stellar component peaks at *H* band and declines rapidly to *V* band. (There is another, much brighter, star about 3″ to the southeast, GSC-2 S011202199954 = USNO-B 0237-0061773, but that is not the optical counterpart and it is not detected in the mid-infrared.) The turn-off mass of the cluster NGC 1978 is estimated to be between 1.44 and 1.49 $M_\odot$ (Mucciarelli et al. 2007). This should also be the original mass of this PPN if it is a member of NGC 1978. According to the stellar evolution models of Karakas et al. (2002), it is not expected that a star of this initial mass will become a carbon star. In the models of Marigo & Girardi (2007) the turn-off mass of NGC 1978 is very close to or slightly smaller than the predicted LMC minimum carbon star progenitor mass, which is between 1.46 and 1.47 $M_\odot$.

This object was classified as a carbon star by Trams et al. (1999) based upon an *ISO* CAM-CVF (Camera Circular Variable Filter) observation. The feature at 11 μm was attributed to SiC emission instead of UIRs. This is clearly not the case from the IRS spectrum. It was suggested to be a post-AGB object by van Loon et al. (2005) on the basis of its near-infrared colors.

SAGE J053525.86−711956.6. There is no optical counterpart to the infrared source. The near-infrared photometry gives $J - K$ of ∼2 mag, which is somewhat larger than is the case for the other objects in the sample, but there is no particular indication from the IRS spectrum that the dust shell has a higher optical depth than for the other sample objects. The spectrum plotted in Figure 1 for this object is similar to that of J051828 and also is reminiscent of the *ISO* spectrum of the Red Rectangle (HD 44179). Clearly, though, this star is more obscured than is HD 44179 given the lack of an optical detection.

The mid-infrared spectrum probably shows a very weak 21 μm feature at low signal-to-noise ratio, but it also seems to show a broader feature on the spectrum from 19 to 22 μm under the nominal 21 μm feature, causing the upturn in the spectrum at 18.5 μm before the start of the 21 μm feature. This broader feature may be related to the adjacent 30 μm feature and

may be some type of weak shoulder on the 30 μm feature or a secondary feature of the carrier. Another possibility is that this is the amorphous carbon continuum shape over these wavelengths, although a "bump" over this relatively restricted wavelength range does not correspond to a blackbody function or to the continuum shape expected from amorphous carbon grains. For this reason we consider it less likely that this is the shape of the underlying amorphous carbon continuum, although we cannot distinguish between these two possibilities with the data that are available.

SAGE J053632.56−701738.4. There is an optical counterpart; however the $V - I$, $B - V$, and $U - B$ colors (+0.7, +2.5, and −0.8, see Table 4) are odd and may indicate a problem in the photometry. The ratio of optical to infrared emission in the SED suggests a moderately high optical depth for the dust shell.

This object and SAGE J055311 have unusual IRS spectra which suggest that they are carbon-rich PPNe, but which are different from the mid-infrared spectra of any previously known PPNe or PNe. The spectra show a very strong feature peaking at ≈11 μm with a weak 11.2 μm UIR feature on top. This feature is discussed further in Section 3.4. While it appears to be SiC, the strength of the feature is quite unprecedented in a carbon star spectrum in the Galaxy or in the Magellanic Clouds. At longer wavelengths there is structure on the continuum but the features are not recognizable. These two objects also have the largest $K - [24]$ colors in the sample, about 1 mag and 0.7 mag larger than for any of the other objects for J053632 and J055311, respectively.

SAGE J055311.98−701522.7. There is a faint optical counterpart close to the SAGE position, but the position difference is large enough (1″, where <0.″5 is usual) that the identification with the SAGE and 2MASS object is tentative. There are some inconsistencies between the photometry reported for this nominal optical counterpart in the literature. The USNO-B and GSC-2 optical magnitudes are not consistent with the MCPS V magnitude, and the DENIS and MCPS I_c magnitudes are also not consistent.

This spectrum is similar to that of J053632, and it is assumed that the strong feature near 11 μm is due to SiC, although again it is much stronger than what is observed in carbon stars in the Galaxy or in the Magellanic Clouds. In this object there appears to be a weak 30 μm feature on the long-wavelength continuum.

SAGE J055825.96−694425.8. There is a relatively bright optical counterpart to the infrared source, detected in the MCPS, USNO-B, and GSC-2 surveys. The short-wavelength SED for this object rises from K band to V band and then declines rapidly to U band, implying that there is a large change of extinction with wavelength across the optical band. This suggests that the dust shell has smaller dust grains than is usual for these 21 μm objects.

The two epochs of *Spitzer* photometry for this object show more variation than is usual for PPNe: the IRAC photometry for the [3.6] and [4.5] filters differs by ∼0.3 mag between the two observations. The IRS spectrum shows no 30 μm feature and, as mentioned earlier, no 21 μm feature either. The IRS spectrum is very similar to the *ISO* spectra of IRAS 07027−7934 and IRAS 21282+5050 in the 5–25 μm wavelength range (see Section 4.1). The UIR plateau feature extends to ∼19.7 μm whereas typically it only extends to ∼18 μm in the other objects.

There is structure in the long-wavelength section of the IRS spectrum which may be due to crystalline silicates. This along with the general nature of the spectrum suggests that the dust shell has a mixed chemistry, as discussed in Section 4.1.

IRAS F06111−7023. This object has no IRAC or MIPS observations as it is located just outside the SAGE survey area. The IRS spectrum was taken at position $\alpha = 06^h10^m32\overset{s}{.}00$, $\delta = -70°24'40\overset{''}{.}6$ (J2000). The IRS position agrees well with the position of IRAS F06111−7023 and also with the position of *MSX* source G280.8021−28.8524, which appears by comparison of the photometry to be the same object as the *IRAS* source. Thus, it is clear that the *IRAS*, *MSX*, and IRS sources are the same object. The IRS position is ∼0.″2 from the 2MASS source J06103202−7024408, which is also DENIS J061032.0−702440. There is an MCPS object close to the 2MASS position. The MCPS I_c magnitude is 1.8 mag fainter than the DENIS I_c observation, which is puzzling. Otherwise the photometry from the MCPS and from DENIS/2MASS produces a well-defined shape for the shorter wavelength SED. The nominal optical counterpart from the MCPS is of magnitude >20 in the U, B, and V filters. The optical counterpart is too faint to be included in the USNO-B or GSC-2 catalogs.

3.4. SiC Features in LMC 21 μm Spectra

The 11 μm SiC emission feature is commonly observed in the mid-infrared spectra of carbon stars, and it is observed as an absorption feature in the spectra of the highest optical depth carbon-rich dust shells (especially in the LMC; see Gruendl et al. 2008). The SiC feature has never been clearly detected in the mid-infrared spectra of Galactic PPNe, although there are a number of instances where PPNe show silicate emission features. Among the carbon-rich PPNe and PNe observed with *ISO* only IC 418 and NGC 6369 show a broad emission feature near 11 μm, but the shape of the feature and the central wavelength do not match the range of commonly observed SiC profiles seen in carbon star spectra. So while the feature observed in these two PNe is likely a variant of SiC emission, the identification is open to debate. In the LMC, a significant fraction of PNe with *Spitzer* IRS spectra show the SiC emission feature combined with the UIR features (Bernard-Salas et al. 2009).

The identification of SiC features in these spectra is complicated by the presence of the UIR emission including the 11.2 μm peak and the associated plateau to longer wavelengths, which obscure the shape of any SiC features that might be present. One is faced with identifying the feature primarily on the basis of its shape on the short-wavelength side up to 11 μm.

Figure 4 shows a comparison of the spectra of J050603 and of J010546. The latter object was chosen for comparison because it has strong UIR features. The dashed lines mark wavelengths 9.0 and 11.0 μm. The spectrum of J010546 has a minimum at 10 μm between the 7.7/8.6 and 11.2 μm UIR features and is rising sharply at 11 μm. The spectrum of J050603 has a very different spectral shape in the 9–11 μm region with a rise starting at 9 μm to what appears to be part of a feature which then merges into the UIR emission at 11 μm. It is this difference in shape which leads us to propose that the "shoulder" extending below 11 μm is part of the SiC feature. For comparison the *ISO* Short Wavelength Spectrometer (SWS) spectrum of a typical Galactic carbon star, V Cyg, is also plotted in the figure.

The shape of this shoulder matches the short-wavelength part of the SiC feature as it is observed in V Cyg. Having an SiC feature along with the UIRs would also explain why the features near 11 μm are so strong in the spectrum of J050603 when the shorter wavelength UIR features are rather weak; in this case most of the emission around 11–13 μm is attributed to the SiC feature rather than the UIR plateau. Examination of the other

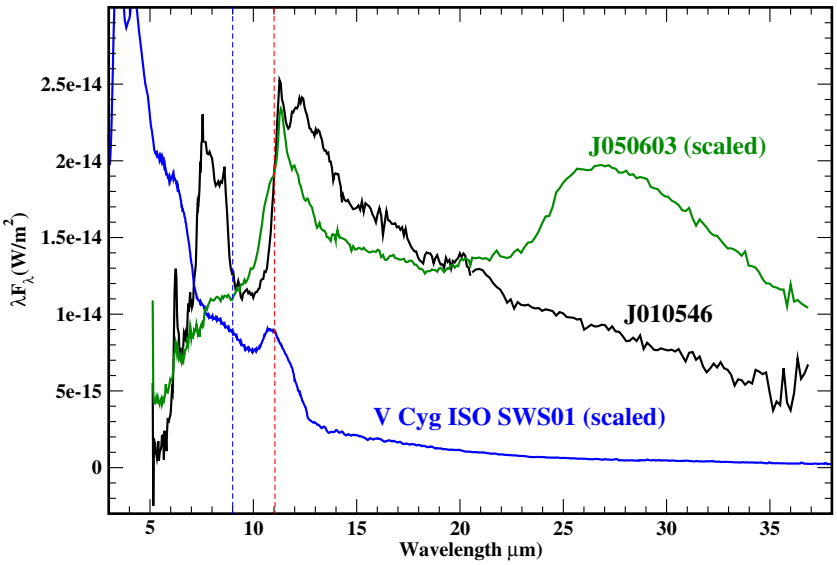

Figure 4. Comparison of the *Spitzer* IRS spectra of J050603 and J010546. The spectrum of J050603 has been scaled down by a factor of about 2.5 to match the general level of the spectrum of J010546. The latter object shows a typical strong UIR spectrum, while the former object shows a feature between 9 μm and 11 μm that we attribute to the short-wavelength part of an SiC emission feature. For comparison the scaled *ISO* SWS spectrum of the bright carbon star V Cyg with a typical SiC emission feature is also shown.

(A color version of this figure is available in the online journal.)

spectra for changes in the continuum shape between 9 and 11 μm as in J050603 resulted in the tentative identification of the SiC feature in three more objects: J050713, J052902, and F06111.

These four spectra in which we tentatively identify SiC emission features also have the most prominent 30 μm features in the entire sample. It is not certain whether this is significant because the two features are generally assumed to have distinct carriers. Objects J051110 and J053525 also have strong 30 μm features but do not appear to have an SiC feature. However, in these cases the UIR emission is quite strong and it is possible that a weak SiC feature may be present under the UIR plateau in each case. The apparent lack of an SiC feature in these two spectra argues against it being directly related to the 30 μm feature.

These four objects with the SiC emission also have similar UIR properties: the 7.7/8.6 μm features are not clearly resolved into two separate features, and the 6.9 μm feature is present. These properties are, however, not exclusive to the subset of objects that appear to have the SiC emission feature, unless the feature is weak and hidden under the UIR features in other objects.

Comparing the 9–11 μm spectral shapes of the Galactic 21 μm objects to those of these assumed SiC emission objects, we find that one object, IRAS 22272+5435, may have an SiC emission feature along with the UIR emission. Only this object appears to have a small shoulder along with the UIR complex around 11 μm in its spectrum, and the feature must be weaker than in these LMC objects if it is present as assumed.

The two unusual objects, J053632 and J055311, have a very strong emission feature near 11 μm. In known carbon stars that show the 11 μm emission feature the maximum feature peak to continuum ratio is about 0.5; this is why in the *IRAS* LRS Atlas the strongest SiC emission objects have classifications of 44 or 45. Only roughly 10% of the carbon star spectra in the LRS Atlas are of class 45. The analogous maximum feature peak to continuum ratio for the 10 μm amorphous silicate feature is >1, and so in the LRS Atlas the strongest silicate emission objects are of class 29. The digit value in the class number is in both cases 10 times the feature peak to continuum contrast (Olnon et al. 1986). The features at ∼11 μm in the spectra of J053632 and J055311 are much stronger than is usually seen for the SiC feature, with feature-to-continuum ratios of ∼1, similar to the strongest observed silicate emission features. The peak wavelength of the feature is at 11.65 μm rather than 11.3 μm as is normal for SiC emission, but this may be due to the effect of the steeply rising continuum under the feature.

We have used the interactive continuum fitting capability in the IRAF *splot* command to fit the continuum shape for these two spectra, divide out the continuum, and obtain a better estimation of the true shape of the features. It is found that the feature shapes and peaks for these LMC objects are similar to what is observed in a small number of Galactic carbon stars (UV Aur and TU Tau; see Speck & Barlow 1997). The feature strengths are, however, 2.5–3 times larger for the two LMC objects than for UV Aur and TU Tau. Objects UV Aur and TU Tau are carbon stars with hot companions and have weak UIR features as well as the SiC feature in their spectra (Speck & Barlow 1997). These two LMC objects may therefore also have hot companions that affect the circumstellar dust shell in some way, although the UIR features in the LMC object spectra are relatively weak compared to the assumed SiC feature.

The shape of the feature in these objects, including UV Aur and TU Tau, is somewhat different than the type of SiC feature that is most commonly seen in carbon star spectra. If the bright carbon star V Cyg is used as an example of the "normal" SiC feature (there is some variation in the feature from object to object), then the feature seen in the spectra of objects J053632 and J055311 is more peaked than the normal SiC feature and is about 1 μm wider at the base of the feature.

Five of the nine PNe with 11 μm SiC emission discussed by Bernard-Salas et al. (2009) have very strong SiC features (namely, SMP LMC08, SMP LMC31, SMP LMC58, SMP LMC85, and SMP SMC01). These five PNe show SiC features similar in shape and strength to what is observed in J053632 and

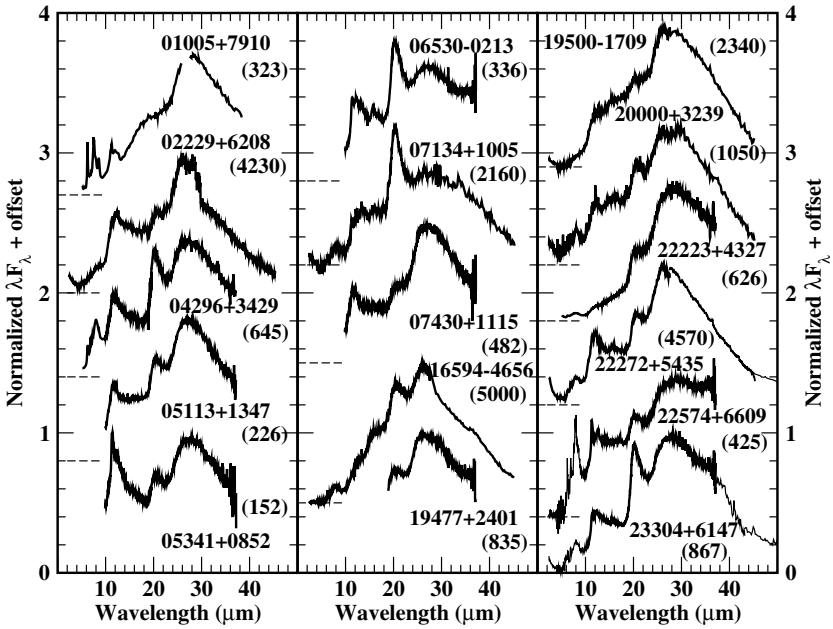

Figure 5. Plot of the normalized *Spitzer* IRS spectra or *Infrared Space Observatory* Short Wavelength Spectrometer/Long Wavelength Spectrometer (LWS) spectra for the Galactic 21 μm sources, along with the carbon-rich PPN IRAS 01005+7910 which lacks the feature but which is included for comparison with the LMC object J051228. As in Figure 1 the peak λF_λ values in units of 10^{-14} W m^{-2} are given in parentheses on the right within each panel. The spectra are generally from Hrivnak et al. (2000), Volk et al. (2002), and Hrivnak et al. (2009). The exceptions are the IRS spectrum of IRAS 01005+7910, from Cerrigone et al. (2009), plus the IRS spectra of IRAS 04296−3429 and 22223+4327 which were reduced from the *Spitzer* archive (*Spitzer* program 00045, PI: T. Roellig). For IRAS 22574+6609 and IRAS 23304+6147, the *ISO* SWS/LWS spectra are shown for wavelengths not covered by the *Spitzer* IRS spectrum.

J055311. This being the case, it is interesting that normal carbon stars in the LMC do not seem to show any SiC features of unusual strength. Where the SiC feature is observed in absorption in the IRS spectra of LMC objects the profile appears to be quite similar to the emission profile in V Cyg and is not as wide or as peaked as is observed in these two PPNe or in the five PNe. Bernard-Salas et al. (2009) note that the SiC feature appears to change as the PNe evolve to higher excitation. This was attributed to photoprocessing of the SiC grains. If that is the case, objects J053632 and J055311 presumably show the feature as it was in the PNe before any photoprocessing took place.

Thus, we tentatively conclude that six of these PPNe possess the 11 μm SiC feature. This is in contrast to the absence of the feature in all save possibly one of the Galactic PPNe. It is not clear why some of these objects and the PNe in Bernard-Salas et al. (2009) have such strong SiC features. This may indicate that these objects have a comparatively large fraction of SiC dust and a smaller proportion of amorphous carbon dust compared to the other objects in the sample.

4. COMPARISON WITH GALACTIC 21 μm OBJECTS

In this section, we compare the mid-infrared spectral properties of the LMC and SMC 21 μm objects to those of the 15 known Galactic objects. Figure 5 shows the mid-infrared spectra of the previously known Galactic 21 μm objects. In this plot, we exclude the small number of other possible, but rather doubtful, 21 μm objects such as the Egg Nebula and IC 418 from the sample. We have included the *Spitzer* spectrum of IRAS 01005+7910 in the figure for comparison with SAGE J051228, even though it does not have a 21 μm feature.

Figure 5 demonstrates that the UIR components in the spectra of the Galactic 21 μm objects are very different from those in the spectra of the Magellanic Cloud objects. For the first 21 μm object discovered, HD 56126 (IRAS 07134+1005), the mid-infrared spectrum shows none of the usual UIR feature peaks (see Kwok et al. 1989; Hrivnak et al. 2000). There is a broad plateau of emission from 11 to 19 μm and a second broad bump around 8 μm. When the object was discovered, the feature peaking near 8 μm was assumed to be a combined 7.7/8.6 μm feature and the longer wavelength emission was assumed to be the same as the extended plateau observed in IRAS 21282+5050 and a few other objects with strong UIR emission (see, for example, Beintema et al. 1996) even though there is no 11.2 μm feature. This initial hypothesis of UIR emission was supported by the observation of a 3.3 μm UIR feature in HD 56126. Subsequent observations have shown that among the Galactic 21 μm objects that have been observed at L band only IRAS 19500−1709 lacks the 3.3 μm feature (Hrivnak et al. 2007), and this object has the weakest UIR-like features in the 5–15 μm wavelength range. A number of papers in the literature have discussed the plateau features as being due to UIRs (i.e., Justtanont et al. 1996; Buss et al. 1990; Volk et al. 2002; Raman & Anandarao 2008), and we will also assume that these plateaus are UIR features. The bump in the spectrum near 8 μm observed in HD 56126 is probably similar to the "class C" 7.7 μm features in the classification scheme of Peeters et al. (2002).

As other Galactic 21 μm objects were subsequently discovered it was found that they show a range of UIR properties. Some of them closely resemble IRAS 07134+1005 in their UIR feature properties, while others have features intermediate between those of IRAS 07134+1005 and those of normal UIR sources. While all of the Galactic 21 μm sources for which spectra have been obtained near 8 μm have a broad 8 μm feature rather than separately resolved 7.7/8.6 μm features, a number of them show the 11.2 μm feature peak and other of the normal UIR features between 11 and 13 μm. These individual features are usually superimposed on a strong underlying plateau, as is also the case for the PN IRAS 21282+5050. Some of these objects also have an unidentified feature at 15.8 μm (Hrivnak et al. 2009).

Overall the UIRs are stronger in the Magellanic Cloud objects, with the peak of the UIR emission often being higher than the peak of the 30 μm feature in Figure 1. This is never the case for the Galactic objects as is seen in Figure 5.

As well as having stronger UIR emission, the Magellanic Cloud objects have more structure in their spectra compared to the Galactic objects. All of the spectra in Figure 3, except that for J050603, where the features are so weak that their structure is difficult to determine, show several of the other individual UIR features even when they have a combined 7.7/8.6 μm feature. Of the 17 objects, 5 have the combined 7.7/8.6 μm feature, 4 show a small 8.6 μm component, and 8 have the 7.7/8.6 μm features clearly resolved as is normal for UIR sources.

The only spectrum in Figure 5 which appears reasonably similar to the bulk of the spectra in Figure 1 is that of IRAS 05341+0852. Even for this object the peak of the 11.2 μm UIR feature is only comparable to the peak of the 30 μm feature rather than being significantly higher as is generally the case for the spectra in Figure 1.

A number of the Galactic objects have very weak UIRs (i.e., IRAS 19500−1709 for example) which have no analog in the Magellanic Clouds sample. The Galactic objects also have higher 30 μm to 10 μm flux ratios compared to the Magellanic Cloud objects, indicating that the dust temperatures are lower for the Galactic 21 μm sources.

The average 21 μm feature strength for the Galactic objects is larger than that observed in the Magellanic Cloud sample in Figure 1. There are not as many objects with rather weak 21 μm features and there seem to be more objects with features of intermediate strength, such as IRAS 05113+1347. Also the Galactic objects with the very strongest 21 μm features such as IRAS 07134+1005 and IRAS 23304+6147 have no equivalents in the Magellanic Cloud sample. It is not clear whether these differences are due to a real difference in the distribution of 21 μm feature strengths in the two samples, or whether it is a result of small number statistics in the samples. The Galactic 21 μm objects were generally first identified as *IRAS* PPN candidates and the feature was observed in the *IRAS* LRS or *ISO* spectra. This may introduce significant selection effects on the Galactic sample that discriminate against objects with weak 21 μm features. On the other hand, one can argue that most of the Galactic sample and all of the Magellanic Cloud samples were originally color selected and that there should not be a significant selection based on the 21 μm feature strength because it does not directly affect the *IRAS* or IRAC/MIPS photometry to any appreciable degree. Figures 1 and 5 together raise the possibility that IRAS 07134+1005, the object often assumed to be the prototypical 21 μm source, is somewhat unusual in its dust shell properties. None of the other 21 μm objects have the combination of a strong 21 μm feature and relatively weak UIR and 30 μm features that is seen for IRAS 07134+1005.

The IRS spectra of objects J010546, J050835, and J055825 show strong similarities to the spectrum of the young Galactic carbon-rich PN IRAS 21282+5050 in the 5–35 μm wavelength range. The *ISO* spectrum of IRAS 21282+5050 is strongly dominated by UIR emission and does not show either the 21 or 30 μm features. The same is true for J055825. J010546 has no 30 μm feature and a borderline 21 μm feature detection. Finally, J050835 shows definite 21 and 30 μm features but these are weak relative to the UIR features. The central star of IRAS 21282+5050 is of type O9, so these three Magellanic Cloud objects might be of a similarly early spectral type. It would be particularly interesting to see whether J050835 is of early B-type or O-type, as no Galactic O-type or early B-type PPNe have the 21 μm feature. Object J051228 of type B0.5I(e) has no 21 μm feature in its IRS spectrum and the dust shell appears more evolved (i.e., the general dust temperature is lower and the optical depth is also lower than for any of the other objects in our sample). The new sample of objects supports the picture that the 21 μm feature becomes strong suddenly in the post-AGB phase and fades out rapidly by the time the star is of early A-type to mid-B-type.

Generally speaking the 30 μm feature strengths of the LMC and SMC objects (Figure 1) are similar to those of the Galactic objects (Figure 5). Where IRS data are available for the Galactic objects, the 30 μm feature shape also appears to be similar for the two groups of objects. One does not seem to see a gradual change in the 30 μm peak position in the sample: IRAS 01005+7910 (B2Iab:e) and J051228 (B0.5I(e)) show similar features shifted to longer wavelengths (29.2 μm), while the rest of the objects all have the feature peaking near 27.5 μm except for J050835 where the feature peak is at 28.4 μm. This behavior of the 30 μm feature implies that it is not affected by the lower metallicity of the LMC compared to the Galaxy, which seems odd if the carrier is MgS since both these elements should scale roughly with the metallicity. On the other hand, the feature definitely seems weaker in the SMC than in the LMC, both for these two PPNe and for the carbon stars observed with the IRS, which would be expected with MgS as the carrier. Where abundance analyses are available for the Galactic objects they are found to be of sub-solar metallicity (van Winckel 2003), so the LMC objects might be of similar metallicity to the Galactic objects, whereas the SMC objects are expected to be of lower metallicity.

4.1. Possible Mixed Chemistry Objects

Six known young Galactic PNe, including IRAS 07027−7934 (PN G291.3−26.2) and IRAS 21282+5050 (PN G093.9−00.1), have strong UIR features but lack the SiC and 30 μm dust features usually observed in carbon-rich PNe. IRAS 07027−7934 has a Wolf–Rayet [WC]-type central star and it also has a circumstellar OH maser (Zijlstra et al. 1991), hence the dust shell has a mixed chemistry. Cohen et al. (2002) analyze the *ISO* spectra of five of these objects, including IRAS 07027−7934, and show that they all have crystalline silicate features in their mid-infrared spectra, at wavelengths beyond 20 μm. No crystalline silicate features have been identified in the mid-infrared spectrum of IRAS 21282+5050 and radio molecular line observations have not detected any oxygen-based molecules around this source, so it is not clear whether this object has a mixed chemistry. However, it shows strong mid-infrared spectral similarities to the other five sources, and the central star has been classified as O-type as well as [WC]-type (see the discussion in Cohen et al. 2002), so there is some uncertainty about the stellar chemistry. It is therefore possible that it, too, has a mixed circumstellar chemistry. Thus, objects similar to IRAS 21282+5050 and IRAS 07027−7934 might be of mixed chemistry, even if we cannot identify crystalline silicate features in their spectra.

Two objects in our sample have spectra of this sort. These sources are quite unlikely to be young YSOs, which often show strongly UIR-dominated spectra in the 5–15 μm range, because in such YSOs the dust continuum is of lower color temperature than in PPNe and PNe, rising to longer wavelengths throughout the IRS wavelength range. These objects are excluded by the selection criteria, and they also have typical ISM UIR emission

spectra that lack the strong plateau under the 11.2 μm feature and extending out to ~18 μm. That type of plateau has to date only been observed in post-AGB objects. While the only way to be 100% certain of the nature of these two sources would be to obtain optical spectra, there is very little chance that they are YSOs.

One of the two objects, J055825, shows some structure in the long-wavelength part of its spectrum that may be crystalline silicate features. The spectrum does not agree well in the overlap region between the short-wavelength and long-wavelength sections, so it is not clear whether the bumps in the long-wavelength spectrum around 21–24 μm are reliable. However, some of these small bumps match the wavelengths of crystalline silicate features observed in IRAS 07027−7934 and similar objects (Cohen et al. 2002).

The other object, J010546, does not show any narrow features in its IRS spectrum from 24 to 30 μm. The structure in the spectrum around 20.6 μm may be due to the presence of a crystalline silicate feature, rather than a 21 μm feature as we have tentatively assumed in this paper, but the other crystalline silicate features at longer wavelengths observed in most of the Galactic objects with similar spectra are not present. Thus, this object is most similar to IRAS 21282+5050 in its spectral properties, and it is not clear why these two objects lack the 30 μm feature, nor it is clear that either of these objects have a mixed chemistry.

It is possible that J010546 is an object of mixed chemistry like IRAS 07027−7934 and the few other Galactic objects of similar spectral properties (aside from IRAS 21282+5050), but that the crystalline silicate features are too weak to observe in its IRS spectrum. Possibly at the lower metallicity of the SMC the silicates have too low an abundance to produce visible features, or do not form at all. However, another possibility is that the lower metallicity of the SMC has affected the formation of the 30 μm feature carrier, so that the object need not have a mixed chemistry to explain the absence of the 30 μm feature. Either molecular line observations or further observations of the dust spectrum are needed to differentiate between these possibilities.

5. RADIATIVE TRANSFER MODELS

Radiative transfer models have been made for most of the objects, with the goal of obtaining basic dust shell properties. The general process of the modeling is the same as has been used in previous papers such as Hrivnak et al. (2000, 2009). The one-dimensional radiative transfer code DUSTCD (Leung 1976) is used to calculate the dust shell models. The inputs to the program include the stellar spectral shape (for which the Kurucz models, Kurucz 1993, are used), the dust optical constants, and the dust density distribution. The stellar temperature is initially assumed to be 7000 K, suitable for an F-type star and if optical photometry is available for the star this value is adjusted to match the observations allowing for the reddening in the circumstellar dust shell. The stellar luminosity was assumed to be 8318 $L_{\odot}$ in the models, which is the expected value for a PPN with a core mass of 0.635 $M_{\odot}$ according to the models of Schönberner (1979). The output model SED was scaled to match the IRS observations at a specific wavelength that represents the continuum without the overlying features. This was usually chosen to be near 18.5 μm, close to the peak of the dust continuum under the features. Thus, the specific luminosity assumed in the model is not important because the model output is rescaled. For each object a distance is found from the model fit, which can be compared to the expected distances of the LMC and SMC. While it would also be possible to fix the assumed distance for each object and vary the luminosity while adjusting some of the other model parameters to produce fits, the model parameters discussed in this paper are independent of the scaling of the model SED.

The method of fitting is to first fit an amorphous carbon dust continuum model to the spectrum and then to add features empirically on top of this base opacity. This is necessary because the 21 μm carrier has not been identified. We also use the same process for the 30 μm feature. While the 30 μm feature is often attributed to MgS grains, we do not have good optical constants for this substance at near-infrared, optical, and UV wavelengths, and there are possible issues with this identification based on abundance arguments (Zhang et al. 2009). The empirical feature shapes for the 21 and 30 μm features come from *ISO* spectroscopy and *Spitzer* IRS spectroscopy of Galactic 21 μm objects, respectively, as discussed by Hrivnak et al. (2009). The dust continuum emission is assumed to be due to amorphous carbon grains of type BE1 from Rouleau & Martin (1991). The grains were assumed to be of radius 0.1 μm by default, although other values of the radius were used if the simulated optical photometry from the models indicated that the optical extinction variation from U to I was not consistent with the observations when using this default grain size. This is mentioned in the discussions of the individual objects to follow. One difference between these models and those for the Galactic objects is that we assume the interstellar extinction along lines of sight to the Clouds to be small, and so we neglect it in the models.

We assumed that there are continuum points in the IRS spectra between the UIRs and the dust features at wavelengths near 5.7, 9.5, and 18.5 μm. These points are critical in the modeling because they determine the maximum dust shell temperature and have a significant effect on the model density profile that is determined. The other important continuum points are the MIPS [70] and IRAC [4.5] photometry points.

The strong UIR features in these spectra present a problem, as these features are generally thought to be produced by single-photon heating, which the DUSTCD code is not able to handle. Attempts to model the UIRs as thermal features by adding in a separate UIR opacity failed because the features were found to become optically thick before they were strong enough to match the observations. We have therefore ignored the UIR features in the fitting but have attempted to balance out the model SED so that the excess infrared luminosity from the UIRs in the observed spectra is matched by an excess in the model luminosity at short wavelengths (<2 μm), thereby producing the correct total flux in the model fit despite not matching the entire infrared spectrum.

If the amorphous carbon dust grains are small enough then single-photon heating would become important for the continuum fitting as well as for the UIR carriers. Where resolved mid-infrared images of the Galactic 21 μm objects are available, analysis of the images and the SED suggest that the dust grains are of size 0.1 μm or larger (i.e., Kwok et al. 2002) for which equilibrium heating models are appropriate. We assume that this is also the case for the Magellanic Cloud objects.

We had more difficulties in fitting the spectra for these new 21 μm objects than was found previously for the Galactic objects. In a number of cases we could not find a power-law density function that produced a good fit to the observations, because when the MIPS [70] photometry was matched, the continuum level near 40 μm was found to be much too low. We found that discrete shells needed to be added to the density

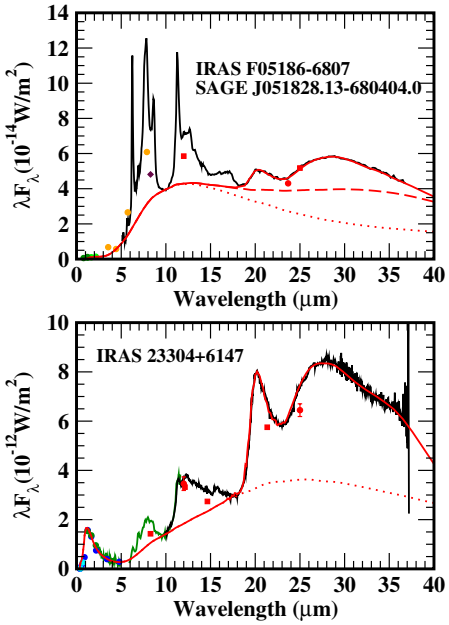

Figure 6. Top panel: the observations of object J051828 are shown as in Figure 1 with the model fit overplotted. The solid curve shows the overall model fit, the dashed curve shows the amorphous carbon continuum fit with the discrete shells to boost the continuum under the features, and the dotted curve shows the corresponding continuum fit with a smooth density distribution. Bottom panel: the *Spitzer* IRS and *ISO* PHT-S (below 10 μm) spectra of IRAS 23304+6147 along with the available photometry are shown with the model fit overplotted. As in the top panel, both the full model fit and the model amorphous carbon continuum from a smooth density profile are plotted to illustrate the difference between the Galactic and Magellanic Cloud models.

(A color version of this figure is available in the online journal.)

Table 5
Model Parameters

Object Name	τ_λ	Relative Feature Strength[a]			T_d (r_{in})[b]	T_*
	(0.55 μm)	21 μm	30 μm	11.3 μm	(K)	(K)
J004441	1.46	0.37	0.37	...	317	6000
J010546	1.15	0.15	0.1	...	271	9000
J050603	15.5	0.09	1.15	0.55	265	7000
J050713	13.8	0.04	0.98	0.5:	242	9500
J050835	27.4	0.30	0.47	...	337	5000
J051110	5.63	0.5	1.55	...	253	5700
J051228	0.82	...	0.7	...	272	30000
J051828	27.7	0.28	0.42	...	258	7000
J051845	4.16	0.60	0.52	...	306	9000
J052043	1.08	0.95	0.88	...	241	5600
J052520	1.52	0.73	0.48	...	241	7000
J052902	9.36	0.12	0.91	0.73	303	6500
J053525	14.0	0.03	0.84	...	215	11000:
J053632[c]	...	...	...	...	...	...
J055311[c]	...	...	...	...	...	...
J055825	1.08	...	...	...	247	14000
F06111	15.5	0.09	1.15	0.4	265	10000:

Notes. Values marked with a colon are uncertain. Typical uncertainties for the model parameters are 0.05 for τ_λ(0.55 μm), 0.01 for the feature strengths, 1 K for the T_d values, and 250 K for the stellar temperature.

[a] The feature strengths in the table are the peak strengths relative to the continuum.

[b] The temperature at the inner radius of the main dust shell. Where a small optical depth hot dust shell is needed to match the 3–5 μm continuum the inner dust shell is excluded.

[c] No good model could be found.

profile in order to produce reasonable fits to the continuum shape in this wavelength range without producing a large excess at longer wavelengths. Figure 6 shows an example of this problem. The IRS spectroscopy and photometry along with the model fit for object J051828 are shown in the figure, along with the model fit (the solid line). The dotted line shows the amorphous carbon continuum that matches the short-wavelength continuum points and the MIPS [70] photometry point with a smooth density profile. The long-dashed line is the adjusted continuum that is needed to fit the spectrum with the 21 and 30 μm features. For comparison a model fit for the Galactic object IRAS 23304+6147 is shown as well. The same fitting process was carried out as for J051828, but for IRAS 23304+6147 the smooth density profile plus the features produces a good fit without needing to add in discrete cool shells to boost the continuum level under the 21 and 30 μm features.

In the most extreme case, we found that the *Spitzer* spectroscopy for J051110 could not be fit by any smooth density profile that we tried, but was fit well using the superposition of two discrete single-temperature layers. This type of behavior in the fits has not been seen before in modeling the Galactic PPNe. Such discrete cool shells cause the SED to be wider in the infrared than is usually the case for models with a smoothly decreasing radial density distribution. This behavior in the SED is commonly attributed to the presence of a disk in the system, as in the case of young stars for example. Thus, the odd density profiles found in these model fits may imply that the assumption of spherical symmetry is incorrect. Another possibility is that the carbon-based dust in the Magellanic Cloud objects has significantly different properties than the BE-type amorphous carbon grains used in these models. We have chosen to use only the BE-type amorphous carbon grains for consistency with the previous models of Galactic 21 μm objects, so that the derived parameters here and in the previous papers can be directly compared to each other.

In the case of object, J050835, we were unable to match the assumed continuum points near 6 and 9.5 μm for any set of model parameters that we tried. The flux ratio between the two points appears to be inconsistent with emission from a blackbody modified by the amorphous carbon opacity function that we are using. This object has extremely strong UIR emission and it may be that the UIR features are so strong that there is no continuum point around 9.5 μm in this case. Alternatively the dust in this object may be somewhat different than in the other objects.

Some objects have a small excess in the 3–6 μm wavelength range compared to what is expected for a stellar photosphere. This type of excess has also been seen in some Galactic PPNe and attributed to warm dust, perhaps from some recent, low-level mass loss. Where such an excess is observed, a small optical depth hot dust component was added to the models to match the near-infrared colors. This was not needed for all objects: for example, J052520 shows no sign of any excess at wavelengths less than 5 μm. Where there is an excess in the observations compared to the model fit only in the IRAC [3.6] filter and not in the *K* or IRAC [4.5] filters, we attribute the difference to the presence of a strong 3.3 μm UIR feature and have not attempted to fit the [3.6] band.

The model parameters are presented in Table 5. Due to the need to use thin shells in the density profiles for many objects, we have not attempted to estimate the mass-loss rates and only present the relative feature strengths, optical depths, and maximum dust temperature values. These parameters should be

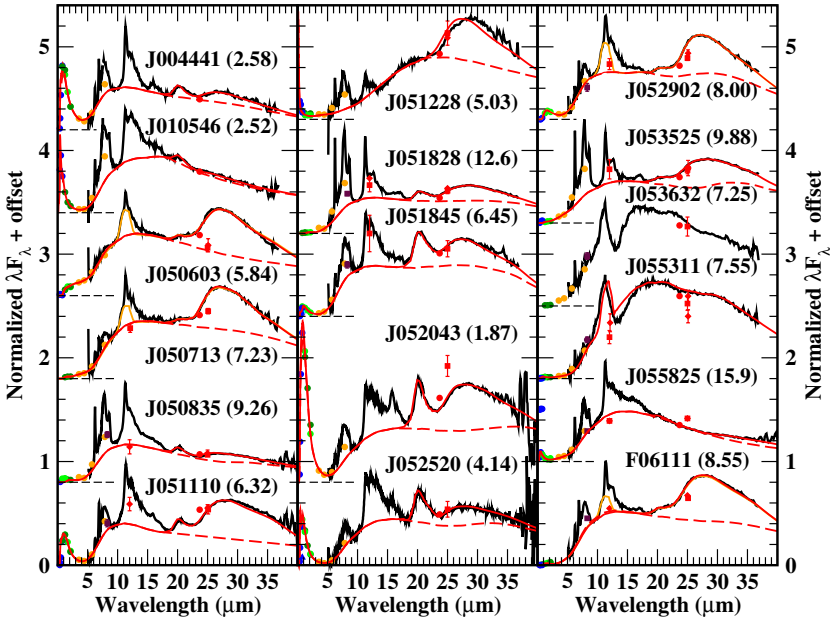

Figure 7. *Spitzer* IRS spectra and photometry are presented for the PPNe as in Figure 1 along with the model fits (solid lines). The dashed curves show the assumed underlying continuum in each model. For J051110 the dust radiative transfer program had difficulty in calculating the continuum model and the result shown appears to be slightly inaccurate. In the four cases where an SiC feature is suspected (J050603, J050713, J052902, and F06111), the fits with that feature included are also shown (orange curves in the color version). For object J055311 the best fit obtained using an SiC feature and an amorphous carbon continuum is shown for comparison with the IRS spectrum; the feature at 11 μm does not match the expected SiC feature shape. The fitting for J053632 was even more difficult and no model that might even be considered as marginally acceptable was found; thus no model results are shown for this object.

(A color version of this figure is available in the online journal.)

robust even when we have unusual density profiles in the model fits. Good quality model fits were obtained for 15 objects but not for the unusual objects J053632 and J055311. The best fit models and the model amorphous carbon continua are shown in Figure 7, along with the observational data exactly as in Figure 1.

For J055311, the closest model fit that was obtained is shown in Figure 7 to illustrate that the V Cyg SiC feature shape, which is taken to be a normal feature shape for carbon stars, does not match the observed feature near 11 μm very well. We attempted fitting the spectrum with pure SiC grains, using the optical constants of Pegourie (1988), and with a combination of SiC grains and amorphous carbon grains coexisting in the dust shell, but in the end the best match we obtained is for amorphous carbon dust grains with the addition of an empirical SiC emission feature derived from the *ISO* spectrum of V Cyg. In effect this is equivalent to assuming that the amorphous carbon and SiC grains both have the same temperature distribution. When using a mixture of the Pegourie SiC and the BE1 amorphous carbon grains in the modeling, we found that when we made the SiC feature strong enough to match the observed feature the dust continuum shape never came close to matching the observed continuum because the SiC grains were always too hot and they produced significant continuum emission at wavelengths <8 μm. For J053632, we also were not able to find a good fit and in this case no model fit is shown in Figure 7.

Similarly, for the objects with more normal SiC features we have made model fits using the empirical SiC emission feature because the attempts that were made to fit the dust continuum with a mixture of SiC and amorphous carbon grains were not successful.

It is difficult to give accurate uncertainties in the model parameters because the fitting process was manual and depends on "by-eye" judgment of the best fit. Within the context of the models, the maximum dust temperature is very accurately determined because small changes in this value shift the continuum level on the short-wavelength side of the peak by a measurable amount. The $T_{\rm d}$ values are accurate to 1 K or less, depending a bit on the actual shape of the observed spectrum. The uncertainties in the other parameters are more difficult to estimate. The feature strengths have an uncertainty of order 0.01, and the $\tau_\lambda(0.55\ \mu{\rm m})$ values have an uncertainty of typically 0.05, if it assumed that the stellar temperature is correct, given typical uncertainties of 0.02 mag for the 2MASS photometry. Finally, in the cases where there is good quality, optical photometry differences in the assumed stellar temperature of order 250 K can affect the quality of the model fit, although for the objects with high optical depths the uncertainty is much larger than this. There are redundancies in the model parameters that make assigning precise uncertainties in the parameters difficult. Given that the models are the result of a manual search of some subset of the parameter space, the uncertainties listed here should be treated with some caution. There are likely to be systematic errors in the parameters because the fundamental dust properties assumed in the modeling are probably not exactly correct.

The general dust properties listed in Table 5 are mostly similar to what are derived for the Galactic 21 μm objects (see Hrivnak et al. 2000, 2009, and other papers referenced therein). The dust shell temperatures $T_d(r_{\rm in})$ are significantly higher than the values derived for Galactic 21 μm objects. The Galactic objects have T_d values in the range 140–220 K, while the values in the models for these new objects range from 215 to 335 K. There are several possible factors that could produce this temperature difference: the PPNe may simply be less evolved off the AGB; the stars might be evolving to high temperatures faster than the Galactic objects, such as due to a higher mass-loss rate in the early post-AGB evolution; the expansion speed of the dust shells may be lower in the Magellanic Cloud objects; or the dust properties may be different in the Magellanic Cloud

Table 6
Percentage of Infrared Emission Carried in Features

Object	UIR 1[a]	UIR 2[b]	UIR Total	21 μm	30 μm	11.3 μm	F_{IR} (W m^{-2})
J004441	7.7	9.3	17.0	1.5	3.9	...	2.26 10^{-14}
J010546	12.0	11.3	23.3	0.6	1.0	...	2.78 10^{-14}
J050603	1.2	5.2	6.4	0.37	11.3	3.3	8.18 10^{-14}
J050713	3.5	4.0	7.5	0.61	12.9	3.1	7.91 10^{-14}
J050835	7.7	10.2	17.9	0.50	3.4	...	7.86 10^{-14}
J051110	4.9	12.1	17.0	1.6	13.4	...	6.51 10^{-14}
J051228	4.8	1.8	6.6	...	13.1	...	5.65 10^{-14}
J051828	14.7	7.3	22.3	1.4	5.5	...	1.24 10^{-13}
J051845	6.8	8.8	15.6	3.8	5.8	...	8.48 10^{-14}
J052043	5.7	9.7	15.4	3.9	11.9	...	2.73 10^{-14}
J052520	3.8	10.0	13.8	4.0	6.2	...	4.12 10^{-14}
J052902	3.4	4.7	8.1	0.50	12.2	4.1	9.23 10^{-14}
J053525	12.4	5,0	17.4	0.13	9.5	...	1.16 10^{-13}
J055825	7.1	11.6	18.7	0.25	...	...	1.40 10^{-13}
F06111	4.2	3.0	7.2	0.30	11.7	1.7	1.31 10^{-13}

Notes. The feature strengths are given as percentages of the total infrared dust emission F_{IR}.
[a] The emission from 5 to 10 μm.
[b] The emission from 10 to 18 μm.

objects. There is some indication from OH maser observations that the wind speeds in oxygen-rich AGB stars in the LMC is smaller than that for similar objects in the Galaxy (Marshall et al. 2004) but it is not known whether this also applies to carbon stars in the LMC. Until more information is available about these objects, particularly spectral types for the stars and molecular line observations to determine the expansion speed of the circumstellar material, we cannot distinguish between these possibilities.

We have calculated the fraction of the total infrared emission in the various features using the IRS spectra and the model fits shown in Figure 7. These were found by integrating over either the IRS spectra (for the UIRs) or the model fits (for the overlapping 21 and 30 μm features), and subtracting off the continuum contribution calculated by integrating the model continuum fits over the same wavelength range. The feature strengths were then converted to percentages of the estimated total infrared luminosity of each object for inter-comparison. We measured the UIR emission between 6 and 10 μm, the UIR emission between 10 and 18.6 μm, the total of all the UIR emission, the SiC feature, the 21 μm feature, and the 30 μm feature. The total infrared flux was found from an integration over the entire IRS spectra range, to which was added the estimated contributions at longer wavelengths and also in the 2–5 μm wavelength range from the model fits. The values are tabulated in Table 6 for the 15 objects with good quality model fits.

With these numbers a quantitative comparison of the feature strengths can be made between the Magellanic Cloud objects and the Galactic objects. Equivalent values to those in Table 6 are given in Hrivnak et al. (2000), Volk et al. (2002), and Hrivnak et al. (2009). The following differences are found.

1. While some of the LMC objects have relatively weak UIR emission, such as J050603, for example, a number of them have very strong UIR features that carry up to 23% of the total infrared emission. Nine of the 15 objects have more than 15% of the total infrared emission in the UIR features. These values are larger than those observed in the Galactic objects.
2. The fraction of energy carried in the 30 μm feature is smaller in the Magellanic Cloud objects than in the Galactic objects. In the present sample the 30 μm feature carries at most 13% of the total infrared energy whereas in the Galactic objects the values range up to 30%.
3. The 21 μm feature carries at most 4% of the total emission in these objects, compared to values of 5%–7% in the strongest of the Galactic 21 μm objects.

Another set of values for the strengths of the various features in the spectra of 10 of the Galactic objects are presented in the recent paper by Zhang et al. (2010), based upon a simpler component analysis of the spectra rather than on dust model fits. That paper gives larger values for the fractional energy of the dust features than are found here because of the way the continuum is fit. While the models in this paper assume a continuum point near 18.5 μm, Zhang et al. (2010) often find the continuum level at this wavelength to be well below the observed spectrum. This leads to larger derived feature strengths for the UIR plateau and the 21 and 30 μm features in that paper compared to what we present here. Nonetheless, the general trends noted above still apply if these values are used for comparison with those in Table 6.

6. NORMALIZED UIR PROFILES

Using the model continuum fits in Figure 7, it is possible to divide the IRS spectra by the model amorphous carbon continuum to obtain ratio plots. In this way the temperature effects in the UIR spectrum will be removed, at least to first order. Figure 8 shows the resulting ratio spectra for the 15 objects with reasonable continuum fits over the wavelength range from 5 to 20 μm. For the sources where there is a suspected SiC feature, Figure 8 also shows the ratio from the model continuum including the SiC feature. The spectrum of the Orion Bar position 5 observed by the *ISO* SWS instrument is shown in the lower left as an example of a typical ISM UIR spectrum. The nebular emission lines in the Orion Bar spectrum have been removed. The 6.3 μm feature in this spectrum peaks at a continuum ratio value of 8.1 so it overlaps a bit with the ratio spectrum of J050835, but it suffices to show how different the

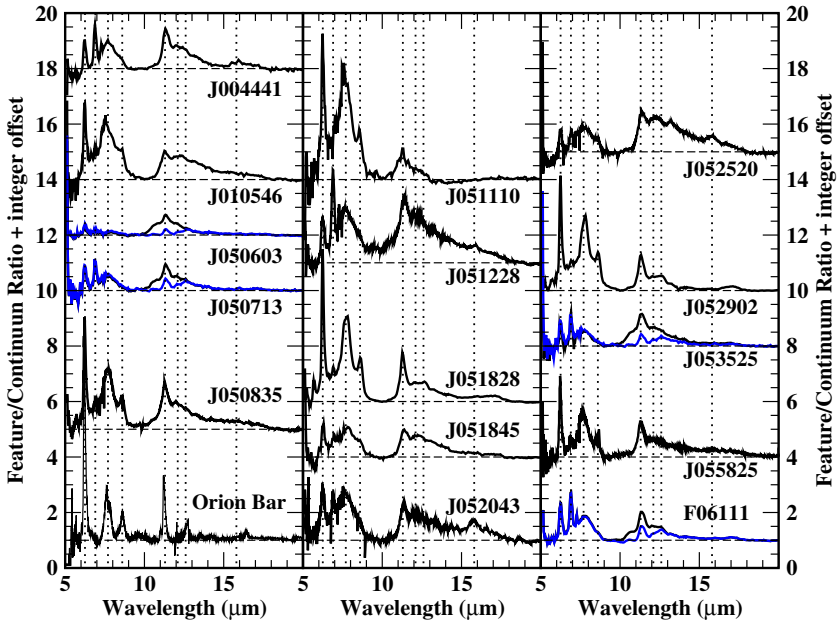

Figure 8. UIR feature-to-continuum ratios are plotted for the 15 objects where good model fits are available. The dotted lines mark the wavelengths of common UIR features. Where the IRS spectrum is suspected to have an SiC emission feature, the ratio curve is shown for both the amorphous carbon only continuum model (black curves) and for the best-fit model continuum with the SiC feature (blue curves). The dashed lines show the continuum levels for the different ratio spectra. For comparison a normalized UIR spectrum of the Orion Bar from the *ISO* SWS instrument is shown on the lower left.

(A color version of this figure is available in the online journal.)

Table 7
UIR Feature Properties

Object Name	Feature Wavelengths (μm)					Feature Classification			
	6.3	6.9	7.7	8.6	11.2	6.3	7.7	8.6	11.2
J004441	6.232	6.882	7.70	...	11.335	B	A′ (C′?)	...	$B_{11.2}$
J010546	6.238	...	7.54	8.60	11.268	B	A′	A″	$B_{11.2}$
J050603	6.244	6.934	7.90	...	11.329	B	B′ (C′?)	...	$B_{11.2}$
J050713	6.241	6.899	7.76	...	11.355	B	B′ (C′?)	...	$B_{11.2}$
J050835	6.225	6.888	7.74	8.55	11.269	B	B′	A″	$B_{11.2}$
J051110	6.242	6.892	7.64	...	11.359	A	A′ (C′?)	...	$B_{11.2}$
J051228	6.246	...	7.59	8.53	11.297	B	A′	A″	$B_{11.2}$
J051828	6.242	6.917	7.80	8.62	11.275	B	B′	A″	$B_{11.2}$
J051845	6.278	6.934	7.83	8.60	11.386	B	B′	A″	$B_{11.2}$
J052043	6.237	6.897	7.64	...	11.330	A	A′ (C′?)	...	$B_{11.2}$
J052520	6.214	6.913	7.63	...	11.338	A	A′ (C′?)	...	$B_{11.2}$
J052902	6.241	6.907	7.80	8.55	11.360	B	B′	A″	$B_{11.2}$
J053525	6.246	6.92	7.81	8.60	11.305	B	B′	A″	$B_{11.2}$
J053632	6.245	...	7.64	8.64	11.26	B	A′	B″	$B_{11.2}$
J055311	6.252	...	7.87	8.67	11.27	B	B′	B″	$B_{11.2}$
J055825	6.232	6.94	7.63	8.61	11.259	B	A′	A″	$B_{11.2}$
F06111	6.255	6.901	7.80	8.58	11.237	B	B′	A″	$B_{11.2}$

Notes. The 7.7 μm feature type is given as A′ or B′ based upon whether the peak wavelength is <7.7 μm or >7.7 μm. In those cases where the 8.6 μm feature is not detected within the 7.7/8.6 profile, the 7.7 μm class may also be C′ if we follow Peeters et al. (2002), but the wavelength is not shifted to ~8.2 μm so this is not entirely consistent with the original class definitions.

UIR emission in these PPNe is compared to what is normally observed in the ISM.

Figure 9 shows the individual features more clearly by overplotting the normalized ratio spectra from 5.5 to 10 μm and from 10 to 19 μm. In Figure 9, the peak height of the 6.3 μm feature above the continuum has been normalized to 1.0 to allow inter-comparison of the relative feature strengths.

We have classified the UIR features in all the sources, including J053632 and J055311, using the scheme of Peeters et al. (2002) and van Diedenhoven et al. (2004), which are based on the peak wavelengths of the features. Table 7 gives the peak wavelengths and classes of the different features. The peak wavelengths are from Gaussian fitting for the 6.3, 6.9, and 11.2 μm features. For the 7.7/8.6 μm features where the shape is decidedly non-Gaussian, the peak wavelengths were determined by eye.

From Peeters et al. (2002) and van Diedenhoven et al. (2004) we would expect for post-AGB objects that the various features will be of classes B, B′, and B″, or possibly class C′ for the 7.7/8.6 complex if these features are blended into a single broad

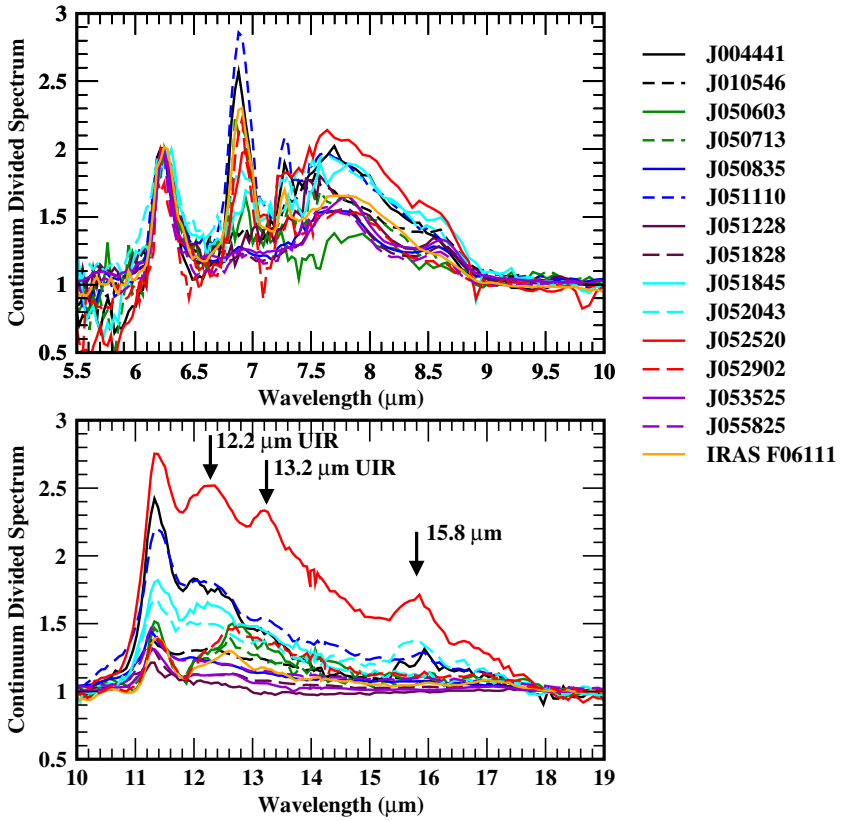

Figure 9. Continuum divided UIR profiles for the objects are shown normalized to a peak height of 1.0 for the 6.3 μm feature. The upper panel shows the short-wavelength region with the 6.3, 6.9, 7.7, and 8.6 μm features. The lower panel shows the 10–19 μm region, illustrating the wide range of relative strengths of the 11.2 μm feature compared to the normalized 6.3 μm features. Additional features are marked at 12.2, 13.2, and 15.8 μm.

(A color version of this figure is available in the online journal.)

feature. For our sample, class B, B′, and B″ features are the most common types but there is a significant minority of class A, A′, and A″ features present.

For the 6.3 μm feature the peak wavelength and shape corresponds to class B in most cases. J050835 and J052520 have peak wavelengths <6.23 μm and on that basis would normally be classified as class A objects. However, in Peeters et al. (2002) the class A 6.3 μm features have a different shape than the class B features, with the latter class being more symmetric in profile. On the basis of the feature shape we have classified the feature as class B in J050835 despite the peak wavelength value. Indeed, none of the objects in our sample have typical asymmetric class A profiles for the 6.3 μm feature, even when the peak wavelength is <6.23 μm and they are classed as class A in Table 7.

For the 7.7 and 8.6 μm features the classification is more difficult. Four sources do not show the 8.6 μm feature, although one could still assume that the feature is present because the combined feature extends to 9 μm. In Peeters et al. (2002), the two objects that did not show the 8.6 μm feature were assigned class C′, but both these objects have the complex at a longer wavelength than for the other sources, peaking at 8.2 μm. All of the Galactic 21 μm sources for which spectroscopy is available from 7 to 9 μm have 7.7/8.6 μm features of class C′ with the combined feature peak shifted to a wavelength between 8.2 and 8.4 μm. In the LMC objects we do not see any wavelength shift in the combined feature, so it is not clear whether these objects should be considered as class C′ or not. We have in all cases assigned classes A′ or B′ based on whether the 7.7 μm feature peaks near 7.6 or 7.8 μm, respectively. We find 8 of the 17 objects are class A′. For the 11 objects where the 8.6 μm feature peak can be measured, 9 are class A″ and 2 are class B″. Thus, the classification of the UIR features based upon wavelength is different between the Galactic and Magellanic Cloud 21 μm sources.

For the 11.2 μm feature the criteria for classes $A_{11.2}$ and $B_{11.2}$ is central wavelengths of 11.2–11.24 μm and ~11.25 μm, respectively. van Diedenhoven et al. (2004) do not give the peak wavelengths for the objects in their sample. What we observe are peak "11.2 μm feature" wavelengths ranging up to 11.37 μm, well beyond the value that is supposed to apply to class $B_{11.2}$. We assume that this still means that the feature is class $B_{11.2}$. All 17 objects are classified as class $B_{11.2}$.

Peeters et al. (2002) and van Diedenhoven et al. (2004) find only a few cases where the various UIR features in a single object show a mix of A and B classes, and where there is a discrepancy it is usually only the 6.3 μm feature that does not match. (We do not consider the 3.3 μm feature because none of our targets have spectroscopy in L band.) In our sample there appears to be more variation between the 7.7 and 8.6 μm feature classification than is observed in the Galactic sources.

The normalized feature profiles allow a measure of the feature strength that is independent of distance. For comparison with Galactic 21 μm objects, the feature peaks near 8 and 11 μm relative to the continuum can be measured and compared with the values given for eight of the Galactic objects in Table 4 of Volk et al. (2002). The average feature strength of the combined 7.7/8.6 μm feature in the Galactic objects is 4.1 ± 2.0 and for the

11.2 μm feature and the underlying plateau the corresponding average value is 0.50 ± 0.22. For the LMC objects the values are 1.63 ± 1.13 and 0.99 ± 0.49, respectively. For the two SMC objects the values are 1.5 ± 0.7 and 1.2 ± 0.3. Thus, the feature strengths vary between the Magellanic Cloud and the Galaxy, with the 7.7/8.6 μm complex stronger in the Galactic objects whereas the 11.2 μm feature and the underlying plateau are stronger in the Magellanic Cloud objects. The average 6.3 μm feature peak value in ratio to the continuum is 1.4 ± 0.7 in the LMC objects, 1.2 ± 0.3 for the two SMC objects, and 0.48 ± 0.45 for the Galactic objects for which observations are available. These values are consistent within the rather large uncertainties. It is clear at least that the range of 6.3 μm feature peak values in the LMC objects is much larger than what is observed in the Galactic objects, and the same appears to be true of the mean feature strength.

Finally, it is possible to integrate under the UIR features after subtracting off the assumed continuum to see what fraction of the total infrared luminosity is being carried by the features. While this is imprecise because the model continuum fit may be incorrect, the estimate that results is that in the Magellanic Cloud objects 15%–25% of the total dust emission is carried by the UIR features for the objects where the features are prominent. For the Galactic objects the values are generally a factor of two lower than this (Volk et al. 2002, Table 5) even for the sources with the strongest UIR features.

7. OBJECT LUMINOSITIES AND DISTRIBUTION ON THE SKY

The available optical, near-infrared, and mid-infrared data for the objects sample the SED over a wide wavelength range, allowing the total flux to be directly calculated from the available observations. This was done for these carbon-rich PPNe and the resulting fluxes were converted to luminosities assuming distances of 50 kpc for the LMC sources (McNamara et al. 2007) and 60 kpc for the SMC sources (Storm et al. 2004). Assuming that the depth of the galaxies is similar to their projected sizes as seen on the sky, the individual LMC objects might have distances anywhere within ±2 to ±3 kpc of this standard distance, while for the SMC the range of possible distances is probably about half of the range for the LMC. Due to the distance uncertainty, the individual luminosity values are uncertain by ±12% for the LMC objects and by ±5% for the SMC objects.

The "internal" luminosity uncertainty from sampling of the points is small for most of the objects. The only object where it appears that there may be enough emission at short wavelengths (beyond *U* band, in the ultraviolet) to affect the integrated luminosity significantly is J051228. In that case the total flux might rise by as much as 60% if the stellar continuum extends right to the Lyman limit along an extrapolation of the *U* and *B* flux points, according to the model fit for this object. The model fit assumes a relatively high effective temperature for the star compared to what would be expected from the spectral type, so the magnitude of the correction is likely to be smaller than the model fit indicates. For all the other objects the flux at wavelengths shorter than *U* band should be at most 0.1% of the total flux. The long-wavelength flux beyond the MIPS [70] photometry point may increase the total flux by ∼1% for most of the objects, judging from the model fits. For J051228, where the dust is cooler and there is proportionally more emission at longer wavelengths, the flux beyond 70 μm may be as much as 2.5% of the total flux. For the SMC objects, which lack MIPS [70] photometry, integration over the models for wavelengths beyond the IRS range is estimated to increase the total flux by 3.9% and 5.6% for J004441 and J010546, respectively.

The luminosity values are tabulated in Table 8 (without any correction for flux at long wavelengths). If it is assumed that the core mass for these PPNe is typically near mass 0.64 $M_{\odot}$, as suggested by the PN 5007 Å line luminosity function, then the nominal luminosity value would be around 8300 $L_{\odot}$ (Schönberner 1979). Instead we find a range of luminosities from ∼4700 to 12,500 $L_{\odot}$. As noted above these values are too low by a few percent due to emission either at short or long wavelengths not covered by the available photometry.

We have also plotted the sky positions of the objects with respect to the LMC and SMC in Figures 10 and 11. The background images in both cases are the SAGE IRAC [3.6] images with logarithmic intensity scaling. For the LMC objects, the sources are not found along the main bar of the LMC where the stellar density is the highest. Most of the 21 μm objects in particular are in the other regions of the LMC instead of along the bar. For the SMC, with only the two identified carbon-rich PPNe, firm conclusions on the sky distribution cannot be made. Object J004441 is located in the south end of the SMC slightly south of the region of maximum star density. Object J010546 is located to the north just beyond the end of the main body of the SMC.

The group of carbon-rich PPNe discussed in this paper is too small to use in a statistical comparison of the sky distribution with other types of objects, although it qualitatively appears from Figure 10 that the LMC PPNe have an unusual sky distribution. We have therefore attempted to select objects of similar broadband colors as candidate PPNe to expand the sample size. This work will be the subject of a subsequent paper, but briefly we originally used the *ISO* spectra of Galactic PPNe, especially the 21 μm objects, to simulate the IRAC/MIPS colors of these objects and examined their colors on a large number of color–color diagrams in order to find a good color selection criteria for PPN candidates. It was found that a reasonably clean selection could be made using the $K - [8.0]$ versus $K - [24]$ colors. For the LMC, a total of 343 candidate PPNe were selected by this color criteria, and all of the carbon-rich post-AGB objects discussed in this paper are part of this sample. For the SMC a similar color selection produces a sample of 175 PPN candidates. Object J010546 is part of the PPN candidate sample, while object J004441 has colors similar to those of carbon stars in this color–color diagram. The PPN candidate samples for the LMC and the SMC are known to be contaminated by PNe, and there may be a small contamination from YSOs and very dusty evolved stars based upon the colors of these objects in the $K - [8.0]$ versus $K - [24]$ color–color diagram.

Comparison of the brightness values for these larger samples of candidate PPNe to those of the objects with IRS spectra discussed in this paper shows that there is a fairly wide range of mid-infrared brightness in the large candidate PPNe samples and that the objects with spectra are brighter than average within the larger sample. The 15 LMC objects discussed in this paper are in the top 33% of the IRAC [8.0] brightness distribution of the larger sample of candidate objects, while object J004441 in the SMC is within the brightest 15% of the larger candidate PPNe sample in this filter. The values for the MIPS [24] filter are similar. The brightness values in the 2MASS or IRAC [3.6] filters for the objects discussed in this paper are much more average compared to the larger samples than is the case in the mid-infrared. As we expect a significant fraction of PNe in these

Table 8
Observed Total Fluxes and Derived Luminosity, Core Mass, and Progenitor Mass Values for the Magellanic Cloud PPNe

Object Name	Estimated Total Flux (10^{-14} W m^{-2})	Luminosity ($L_\odot$)	$M_{\rm core}$ ($M_\odot$)	$M_{\rm initial}$ ($M_\odot$)
			Marigo & Girardi Models	
J004441	4.20 ± 0.16	4750 ± 420	$0.566^{+0.024}_{-0.007}$	$1.01^{+0.11}_{-0.03}$
J010546	4.12 ± 0.23	4660 ± 510	$0.564^{+0.026}_{-0.008}$	$1.00^{+0.12}_{-0.04}$
J050603	9.12 ± 0.09	7140 ± 930	$0.607^{+0.018}_{-0.014}$	$1.30^{+0.09}_{-0.07}$
J050713	8.25 ± 0.08	6290 ± 820	$0.595^{+0.012}_{-0.018}$	$1.24^{+0.06}_{-0.10}$
J050835	8.37 ± 0.08	6550 ± 850	$0.599^{+0.013}_{-0.016}$	$1.26^{+0.07}_{-0.08}$
J051110	8.55 ± 0.09	6700 ± 870	$0.601^{+0.014}_{-0.015}$	$1.27^{+0.08}_{-0.08}$
J051228	5.37 ± 0.05[a]	4200 ± 550	$0.555^{+0.009}_{-0.011}$	$1.01^{+0.06}_{-0.06}$
	8.84 ± 0.09[b]	6920 ± 900	$0.604^{+0.016}_{-0.014}$	$1.29^{+0.09}_{-0.07}$
J051828	13.3 ± 0.1	10400 ± 1350	$0.678^{+0.052}_{-0.031}$	$1.93^{+0.48}_{-0.46}$
J051845	8.49 ± 0.08	6650 ± 860	$0.600^{+0.014}_{-0.015}$	$1.27^{+0.07}_{-0.08}$
J052043	6.46 ± 0.06	5060 ± 660	$0.569^{+0.014}_{-0.010}$	$1.10^{+0.08}_{-0.07}$
J052520	6.43 ± 0.06	5040 ± 660	$0.569^{+0.014}_{-0.010}$	$1.10^{+0.08}_{-0.07}$
J052902	11.0 ± 0.1	8630 ± 1120	$0.638^{+0.025}_{-0.024}$	$1.44^{+0.30}_{-0.10}$
J053525	12.6 ± 0.1	9890 ± 1290	$0.666^{+0.059}_{-0.029}$	$1.79^{+0.60}_{-0.35}$
J053632	11.4 ± 0.1	8930 ± 1160	$0.644^{+0.027}_{-0.025}$	$1.46^{+0.38}_{-0.10}$
J055311	10.7 ± 0.1	8390 ± 1060	$0.632^{+0.023}_{-0.023}$	$1.42^{+0.26}_{-0.11}$
J055825	16.0 ± 0.2	12500 ± 1620	$0.736^{+0.056}_{-0.013}$	$2.45^{+1.09}_{-0.08}$
F06111	12.6 ± 0.1	9860 ± 1280	$0.665^{+0.060}_{-0.029}$	$1.78^{+0.61}_{-0.34}$

Notes. The luminosity uncertainties include the flux uncertainty and the distance uncertainty for the objects. The Marigo & Girardi (2007) initial and final mass values are derived based on information downloaded from the Padova stellar evolution group Web site, assuming that the tip-of-the-AGB luminosity is the same as the post-AGB luminosity. The Padova stellar models predict that most of these objects should be oxygen-rich rather than carbon-rich at the end of the AGB, contrary to our observations.

[a] Using only the observations.

[b] With an extrapolation to UV wavelengths.

samples, these objects probably are more likely to have smaller IRAC [8.0] and MIPS [24] fluxes because they are more evolved and the dust is cooler. Thus, it is not surprising that the PPNe discussed in the paper are in the top part of the mid-infrared brightness distribution of the candidate PPNe.

For the LMC and SMC SAGE samples, most ordinary types of objects can be identified in any one of several color–magnitude diagrams (Blum et al. 2006). We have used a $J - [3.6]$ versus [3.6] color–magnitude diagram to select various types of stars in the LMC and SMC including K-type giants, oxygen-rich AGB stars, AGB carbon stars, M-type supergiants, and very dusty evolved stars. Where IRS spectra are available for the very dusty star sample, the objects are found to be extreme carbon stars in nearly all cases. The extreme carbon stars, being in the high mass-loss rate "superwind" phase of AGB evolution, are considered to be very near the end of their AGB evolution, so these objects are expected to be the most immediate progenitors of the carbon-rich PPNe. The sky distributions of each of these samples of objects were compared to the PPN candidate samples using the standard non-parametric Kolmogorov–Smirnov statistical test. Due to the relatively small number of objects in the PPN candidate samples, we used the right ascension and declination histograms for the test rather than the two-dimensional sky distributions. For the LMC, the carbon-rich PPNe discussed in this paper are a large enough group that we can attempt a Kolmogorov–Smirnov test between these objects and the set of 343 candidate PPNe. It was found that the two distributions were consistent within the limitations of the small sample size, so we will use the larger sample as a proxy for PPNe in the LMC. We assume that the same holds for the SMC.

The K-type stars in the LMC and the SMC both are found to closely trace the total starlight, being strongly peaked along the main bodies of the two galaxies. The Kolmogorov–Smirnov tests show that the PPN candidates have a different sky distribution than the K-type giants. That is not particularly surprising. What is surprising is that neither the oxygen-rich AGB sample nor the carbon star sample nor the dusty evolved star sample have sky distributions that match the PPN candidates in the LMC or the SMC. The probabilities of a match from the Kolmogorov–Smirnov tests are small, $<8 \times 10^{-5}$ for the LMC tests and $<5 \times 10^{-4}$ for the SMC tests. The oxygen-rich AGB and K-type star samples have distinctly different sky distributions from the carbon stars and the very dusty objects. In the LMC the very dusty objects have a sky distribution that is consistent with the carbon star sample, as expected.

Matsuura et al. (2009) have noted that the sky distribution of typical carbon stars in the LMC is different than that of the subset of the carbon stars with estimated high mass-loss rates ($>6 \times 10^{-6}\ M_\odot$ yr^{-1}), with the general carbon star population being distributed mainly along the bar of the LMC and apparently sampling a lower mass and older population than do the carbon stars of highest mass-loss rate. The sky distribution of the PPN candidates matches better to the subset of carbon stars with high mass-loss rates, rather than to the general carbon star population, although we do not have good

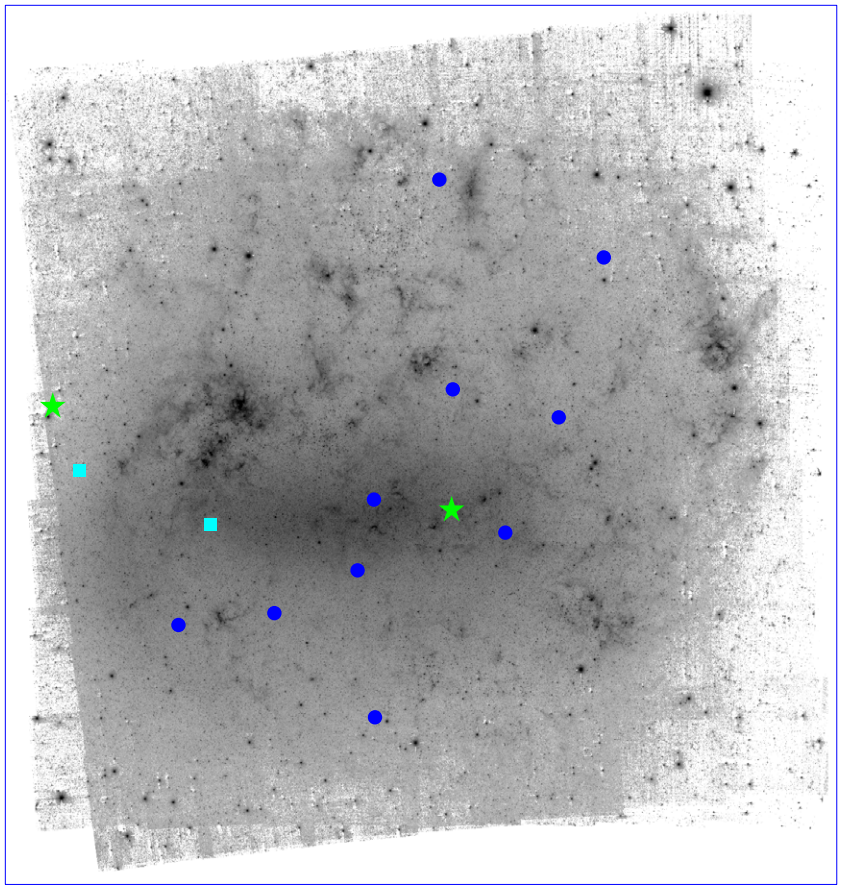

Figure 10. Sky positions of the LMC carbon-rich PPN candidates are shown superimposed on an image ($8\overset{\circ}{.}23 \times 8\overset{\circ}{.}76$) of the LMC in the *Spitzer* [3.6] filter. The image is oriented so the LMC bar runs from left to right. The blue dots show the positions of the 21 μm objects (IRAS F06111−7023 is located off the image to the left), the two green stars mark the position of J051228 and J055825 which have no 21 μm feature, and the two cyan squares mark the positions of the strong SiC feature objects J053632 and J055311. The image is centered at $\alpha = 05^{\rm h}18^{\rm m}48\overset{\rm s}{.}080$, $\delta = -68^{\circ}42'01\overset{''}{.}34$ (J2000) and is rotated -27° east of north.

(A color version of this figure is available in the online journal.)

enough statistics to demonstrate that the PPN and high mass-loss rate carbon star sample objects have the same sky distributions. This suggests that the minimum progenitor mass for the PPNe candidates is higher than the minimum progenitor mass for the carbon star population as a whole, so that carbon stars of lower initial mass do not evolve into PPNe.

8. DISCUSSION

8.1. Frequency of the 21 μm Feature in Carbon-rich PPNe

Out of the 15 LMC/SMC objects that are clearly carbon-rich PPNe, at least 9 objects show the 21 μm feature, and it is possible that the total is 13 if the marginal detections are real. Overall about half of these objects show a reasonably strong 21 μm feature that could be recognized at either lower spectral resolution or lower signal-to-noise levels (as was the case in the discovery of many of the Galactic 21 μm objects from the *IRAS* observations), while the feature is much weaker or is absent in the remaining objects. Considering also that object J051228 has a much earlier spectral type than the other objects in the sample whose spectral types are known, and so would not be expected to have the 21 μm feature based on properties of the Galactic 21 μm objects, it appears that a large majority of carbon-rich PPNe develop the 21 μm feature as they evolve off the AGB. Alternatively, the conclusion from Figure 1 may be that the 21 μm feature develops for all carbon-rich PPNe but is only prominent during about half of the PPN evolution. This question ultimately can only be resolved by obtaining spectral types for the PPNe in our sample to see if the objects with weak features have the same range of spectral types as the objects with stronger features.

As noted in the previous section, we have samples of 343 candidate PPNe in the LMC and 175 candidate PPNe in the SMC based upon color selection. The selection area also is where PNe are detected so there is likely to be a significant fraction of PNe in these 518 objects. However, the selection area was chosen to exclude YSO candidates and other types of objects, such as early-type stars with long-wavelength excesses, that can be identified in other color–magnitude and color–color diagrams (i.e., see the discussion in Blum et al. 2006). Only 0.2% of the YSO candidates identified based upon the $J - [3.6]$ versus [3.6] color–magnitude diagram are in the PPN candidate region in the $K - [8.0]$ versus $K - [24]$ color–color diagram, where they are 20% of the total number of objects. There is clearly a significant overlap between the colors of post-AGB and YSO objects in the $J - [3.6]$ versus [3.6] color–magnitude diagram, and with just the short-wavelength photometry we cannot distinguish the PPNe and PNe from the more numerous YSOs. By choosing the PPNe candidate sample in the $K - [8.0]$ versus $K - [24]$ color–color diagram to exclude the main group of YSO candidates, we should be preferentially selecting the PNe and PPNe. None of these candidate PPNe which have IRS spectra are found to be YSOs; they are all found to be PPNe

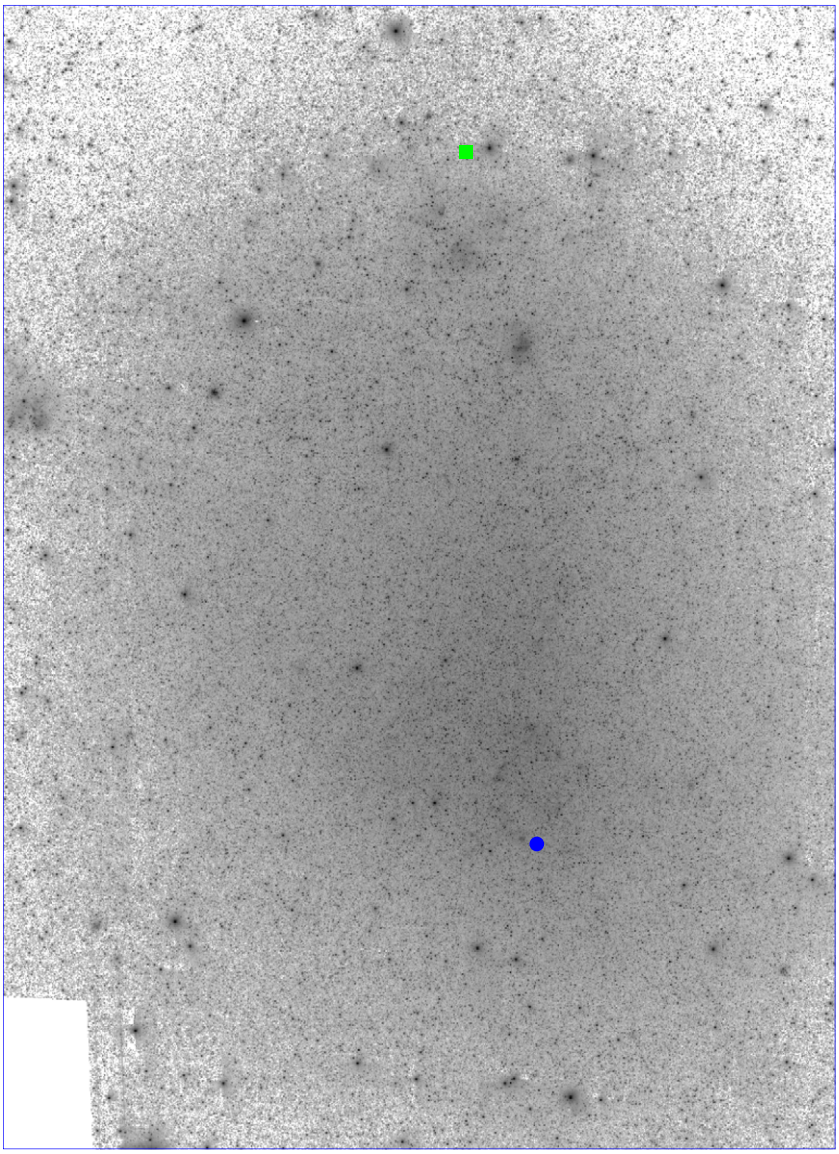

Figure 11. Sky positions of the two SMC carbon-rich PPNe are shown superimposed on an image (4.°44 × 6.°11) of the SMC in the *Spitzer* [3.6] filter. The image is oriented so the Magellanic Stream runs off to the left of the image, hence the vertical axis runs from northeast to southwest on the sky (top to bottom). The blue dot shows the position of the 21 μm object J004441. The green square marks the position of the other carbon-rich PPN J010546 which may have a weak 21 μm feature. The image is centered at $\alpha = 00^{\rm h}56^{\rm m}17^{\rm s}.155$, $\delta = -72^{\circ}57'10''.23$ (J2000) and is rotated $-31.^{\circ}6$ east of north.

(A color version of this figure is available in the online journal.)

as expected. Hence, we believe that the YSO contamination is actually much less than 10% of the sample. It is of course possible that some PPNe are excluded in this selection due to our effort to exclude YSOs and other known types of objects, so the true sample of PPNe in the Magellanic Clouds may be larger than assumed here. We have found 5 oxygen-rich PPN or PN candidates in the IRS spectra of LMC and SMC objects that are publicly available from the *Spitzer* archive, along with the 17 carbon-rich PPN candidates discussed in this paper. If these numbers are representative of the larger sample, and if we assume that half of the 518 candidate objects are PNe, then the number of PPNe in the LMC and SMC is roughly 260, of which about 200 will be carbon-rich and the remaining 60 will be oxygen-rich. If 75% of the carbon-rich PPNe show the 21 μm feature, there would be ∼150 such objects in the LMC and SMC. This number is uncertain, but it indicates that the sample here is only a small fraction of all 21 μm objects in the Magellanic Clouds.

If there are dozens to hundreds of 21 μm objects in the LMC and SMC as this rough estimate suggests, there should be a much larger population of 21 μm objects in the Galaxy—other things being equal—because the Galaxy is much more massive than the Clouds. Most of the known Galactic 21 μm objects (13 out of 15) are found in the outer Galaxy. This differs from the galactic longitude distribution of all PPN candidates in the Torun post-AGB catalog, where a large fraction of the sample is located in the inner Galaxy (Szczerba et al. 2007, their Figure 2). We know of a small number of candidate carbon-rich PPNe from the *IRAS* mission that do not have the 21 μm feature even though their general properties appear to be similar to the 21 μm objects. We know of additional carbon-rich PPN candidates with early spectral types that also do not show the 21 μm feature. It is difficult to determine what fraction of the carbon-rich PPNe in the Galaxy of intermediate spectral type have the feature, but overall the fraction of 21 μm objects in, for example, the carbon-rich objects listed in the Torun post-AGB list is relatively small.

Where abundance analyses are available for the Galactic 21 μm objects they are found to be of lower than solar initial metallicity, roughly from −0.5 to −1.0 solar, although they show large enhancements of the *s*-process elements. This range of metallicities overlaps with the metallicities of the Magellanic Clouds. It may be that in this range of metallicity the 21 μm objects are more efficiently produced, and therefore that such objects are more easily found in the Magellanic Clouds where there is not such a wide range of metallicities as is the case in the Galaxy. Nonetheless, it still seems odd that a small spectroscopic survey of objects in the Clouds have discovered as many 21 μm objects as are currently known in the Galaxy where many more mid-infrared spectra have been obtained.

8.2. UIRs and Carbon-based Molecules

The UIR features generally appear quite strong in the spectra of these Magellanic Cloud PPNe. As discussed previously, the features are typically twice as strong as in the Galactic 21 μm objects. A basic question is whether this difference is due simply to a higher abundance of the carrier, presumably PAHs, or whether it implies a difference in the excitation process. In the ISM the UIR emission is generally assumed to be due to ultraviolet excitation of the molecules followed by fluorescence. When the UIR features carry ∼20% of the total infrared emission, as is the case for the Magellanic Cloud objects with the strongest UIR emission, this means that the PAHs need to be absorbing ∼20% of the stellar light that is heating the dust shell. For a star of spectral type F5 and effective temperature 6600 K, only 4% of the total luminosity is radiated at wavelengths <3500 Å, so the UV part of the spectrum carries too little energy to excite the UIR features that are observed, even if 100% of the UV radiation is absorbed by the PAHs. Wavelengths <4400 Å carry 20% of the total luminosity for stars of this type. Thus, the UIRs must be excited by a combination of optical and UV radiation. That behavior is expected to occur when the PAHs are large: containing hundreds of C atoms rather than being small clusters with ∼40 C atoms (see the review by Tielens 2008). Probably both factors are involved in producing the strong UIR emission—the generally lower initial metallicity of the Clouds allows the AGB stars to dredge up enough carbon to produce large C/O ratios, and this in turn may allow more and larger PAH molecules to form and be excited more strongly by a star of intermediate spectral type. If it becomes possible to carry out an abundance analysis on one or two of the optically brighter objects, it would be interesting to see whether the C/O ratio is larger than that found for the Galactic 21 μm sources.

As discussed in Section 6, the objects show more variation in the shapes and strengths of the 7.7 and 8.6 μm features than is observed in carbon-rich PPNe in the Galaxy. In addition, the great strength of the 6.9 μm feature in some of the spectra is something that is not seen in Galactic PPNe. We do not understand the details of the formation of the features well enough to determine the exact cause of these variations in the UIR features. Spectroscopy of the 3.3/3.4 μm features would be valuable to see whether these features also show new properties compared to Galactic objects. The objects are faint enough that an 8 m class telescope would be needed for such observations, but they are possible.

8.3. Correlations between the Parameters and the Spectral Features

We have attempted to find correlations between the various model parameters given in Table 5 and the strengths of the different features seen in the IRS spectra given in Table 6. Plots of each of these quantities against all of the others were made, and no strong correlations were found. Only two possible weak correlations were found: there is some tendency for higher stellar temperatures as deduced from the models to go along with weaker 21 μm features, and there appears to be a weak anti-correlation between the 30 μm feature strength and the total UIR emission. The first of these correlations is consistent with the general observation that few hot PPNe in the Galaxy have the 21 μm feature, although IRAS 16594−4656 is one example that is contrary to this idea. The second correlation, if it is significant, is something that has not been suggested for Galactic PPNe.

Figure 12 shows the plot of the 30 μm feature strength in % of the infrared luminosity versus the total UIR feature strength in the same units. A linear correlation fit to these data produces a Pearson correlation coefficient of −0.737 for the 15 points. This is nominally significant at the 2.1σ level. The non-parametric Spearman rank test assigns the correlation a significance of 2.0σ. Either way, the correlation is a borderline result. One possible interpretation of this result and the lack of any correlation of either quantity with the estimated stellar temperature is that there is some competition in forming the UIR and 30 μm carriers, so that when more of one of them is formed then less of the other is formed. In general terms, this suggests that the gas-to-dust mass ratio is varying between the different sources, and that where there are more PAH molecules to produce the UIR features there is less dust and the 30 μm feature is weaker. In the context of the idea that the 30 μm feature is due to amorphous carbon grains coated with MgS (Hony et al. 2002), there may be competition between forming the amorphous carbon grains and forming the PAHs.

8.4. Luminosity of the Objects

Models of AGB and post-AGB evolution predict that for AGB and post-AGB stars there is a well-defined relationship between the core mass and the luminosity just before a thermal pulse. Models of post-AGB evolution (Schönberner 1979; Blöcker 1995) also predict that the rate of post-AGB evolution is a very strong function of the core mass and the mass-loss rate, such that lower core mass objects evolve very slowly and probably cannot illuminate a PN. This is because the circumstellar shell will disperse before the star becomes hot at lower core masses. The high core mass objects are expected to evolve so quickly that the PPN and PN phases are very brief and unlikely to be observed. The distribution of white dwarf masses and the initial–final mass diagram, when combined with these results of the stellar evolution models, leads to predictions about the luminosity of post-AGB objects. Due to the combination of the sharply peaked distribution of white dwarf masses and the large change of post-AGB evolution rate with the core mass, most observed post-AGB stars are expected to have masses around 0.6–0.64 $M_{\odot}$ and luminosities that match these core masses: between 7000 and 8500 $L_{\odot}$ according to the Schönberner and Blöcker models (the more recent Karakas et al. 2002 and Marigo & Girardi 2007 models predict lower luminosities for these core masses). The Blöcker models have higher assumed post-AGB mass-loss rates and thus more realistic timescales for the post-AGB evolution. Post-AGB objects with much higher core masses are expected to be significantly brighter but have much shorter transition times between the AGB and the white dwarf cooling track, and also are expected to be more obscured by their circumstellar shells at the end of the AGB. Thus, there

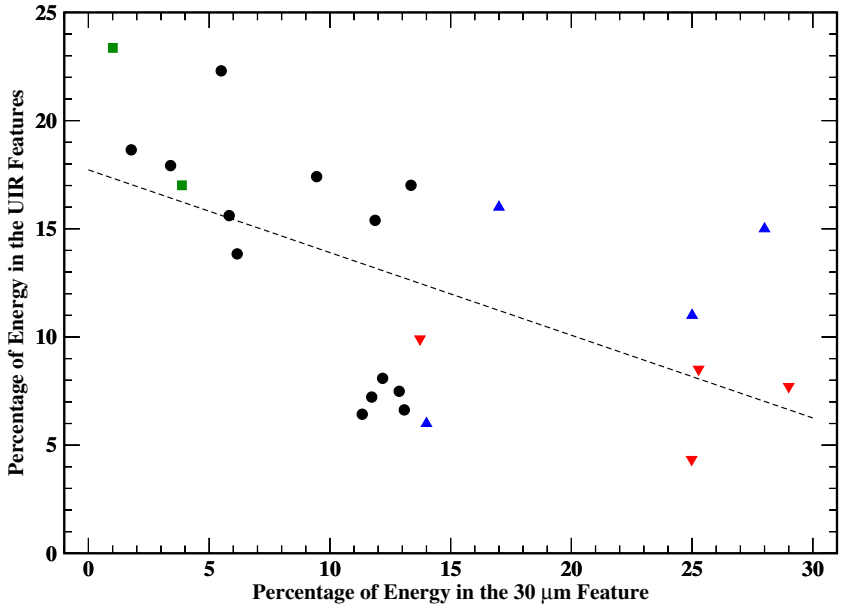

Figure 12. Percentage of the infrared emission in the 30 μm feature is plotted against the percentage of the infrared emission in the UIR features. Different sets of objects are plotted with different symbols: LMC objects (circles), SMC objects (squares), Galactic 21 μm objects re-fit the same way as the Magellanic Cloud objects (down triangles), and Galactic 21 μm objects with fits based on *ISO* spectra (from Hrivnak et al. 2000; up triangles). The dashed line shows the derived (weak) correlation function.

(A color version of this figure is available in the online journal.)

is less chance of finding such massive post-AGB objects in brightness-limited samples in the Galaxy.

For the *Spitzer* surveys the situation is a bit different. Any PPNe in the Clouds with dust luminosities of $\gtrsim$500 $L_{\odot}$ and in the survey area will have been detected—to take a very conservative limit from the dust radiative transfer models given the known detection limits of the SAGE survey. Some unknown bias is introduced by the selection of objects for IRS spectroscopy, but in general we should not have any bias against detecting the more slowly evolving PPNe. Assuming that the initial–final mass relation is the same in the Clouds as in the Galaxy, we expect most objects to be in the 6000–9000 $L_{\odot}$ luminosity range. We would not expect to detect a large fraction of high-luminosity objects because they are comparatively rare due to the initial mass function and their faster post-AGB evolution. Higher luminosity objects are likely to have a detection advantage at in flux-limited mid-infrared surveys in the Galaxy, because they are visible over a larger fraction of the disk than the lower luminosity objects are for a given minimum detection limit, but this is not the case for the Magellanic Cloud objects observed by *Spitzer* since all the objects are expected to be well above the detection threshold.

There is a general trend in the sample that objects with lower luminosity have lower dust luminosities as well, and thus have lower optical depths in the model fits. The exceptions are objects J050603, J050713, and J050835, which have moderate luminosities but no optical counterparts. In general we would expect the lower luminosity PPNe to have less massive dust shells, both because the mass-loss rate appears to increase with the luminosity and because the slower PPN evolution of the lower mass objects allows the dust shell more time to disperse. This matches the general trend in our sample.

It is also possible for a sample of PPNe with the same intrinsic luminosities to produce a range of observed fluxes if they have an asymmetric disk-like dust shell with bipolar lobes. In such cases the disk obscures the star much more when we happen to observe the system edge-on than if we happen to be looking down one of the lobes. This type of structure is observed in many Galactic PPNe. The carbon-rich PPN IRAS 17441−2411 is an example of the nearly edge-on case (Su et al. 1998). This type of dust shell geometry produces a trend that when we view the object edge-on, then it has a faint optical counterpart, too low a derived luminosity, and too large a fractional dust luminosity. When such bipolar objects are viewed more nearly along the poles the stars are visible, the fraction of dust emission is lower, and the luminosity is somewhat overestimated. That is the opposite of the general trend observed in our sample, but for the objects J050603, J050713, and J050835, which have no optical counterparts, this type of geometric effect may be causing the luminosity to be underestimated. For the other objects in the sample, if there is an effect due to bipolar structure it would increase the luminosity range rather than reduce it.

We conclude that the large range of luminosities observed in these PPNe is intrinsic. A similar wide range of estimated luminosity is found for samples of carbon star candidates selected based on their photometric colors (Blum et al. 2006) in the LMC and SMC. The implication would appear to be that the post-AGB evolution timescale is not as sensitive to the core mass, and hence the luminosity, as some of the stellar evolution models indicate. We see a relatively flat distribution of luminosities from around 4500 to 12,500 $L_{\odot}$ in the sample, subject to the uncertainties of small number statistics. Due to the initial mass function and the shorter post-AGB evolution times for more massive remnant white dwarf stars, the stellar evolution models predict that the higher luminosity PPNe should be much rarer in any complete sample than the lower luminosity objects.

The large range of luminosity is also interesting in that the lowest luminosity objects are below the estimated minimum progenitor mass (2.3 $M_{\odot}$) for carbon stars in the Magellanic Clouds according to the models of Karakas et al. (2002). This problem is discussed by Girardi & Marigo (2007) and Marigo & Girardi (2007), who present the results of synthetic AGB

models which give a mass range of 1.5–2.8 $M_{\odot}$ for carbon star progenitors in the LMC. The better match to the cluster turn-off mass in NGC 1978 is not surprising because they base their models on observations of carbon stars in NGC 1978 and other LMC clusters. The Marigo and Girardi papers do not give enough information in the text for us to compute the predicted progenitor masses for different luminosities. However, using isochrones from the Padova group Web site http://stev.oapd.inaf.it/cgi-bin/cmd_2.3 under the assumption that the post-AGB luminosity is the same as the AGB tip luminosity, we have found the initial mass and final mass values that correspond to the luminosities calculated for our objects. These values are given in Table 8. We have applied the uncertainties in the integrated flux discussed above to the values and give the range of core masses and initial masses from the Padova models in the table.

We also attempted to generate core mass and initial mass values from the Karakas models. However the Karakas et al. (2002) and Izzard et al. (2004) papers do not tabulate the initial–final mass relation in the models. We attempted to use the initial–final mass relation from Catalan et al. (2008), which was derived from observations of white dwarf stars in the Galaxy, along with the Karakas model parameterizations to find the progenitor masses of the objects in our sample, but we found that while the estimated core masses were similar to the values from the Padova group models the initial masses from the Catalan et al. (2008) relation were significantly higher than what the Padova models predict. The difference is 0.6–1.0 $M_{\odot}$. As it is not clear that the Galactic initial–final mass relation also applies to the Magellanic Clouds, we have therefore not tabulated these values in Table 8.

In the Padova isochrones there is a difficulty in that the minimum initial mass for carbon stars at the LMC metallicity is predicted to be between 1.46 and 1.47 $M_{\odot}$, so the models predict that 9 of our 15 LMC PPNe should be oxygen-rich from the values in Table 8. Object J052902 has a derived initial mass of $1.44^{+0.30}_{-0.10}$ $M_{\odot}$ which is consistent within the uncertainties with the turn-off mass of NGC 1978 and with the star being carbon-rich, but most of the uncertainty in the luminosity, and hence in the initial mass, is due to the uncertainty in the position of the object within the LMC. If one assumes that there is a 50% chance that the object is at a distance of 50 kpc or less, then there is a 50% chance that the object is predicted to be oxygen-rich by the Padova models. Two other objects, J053632 and J055311, have masses near the minimum carbon-star progenitor mass in the Padova models. Only three objects are found to be clearly luminous enough that they are predicted to be carbon-rich by the Padova models.

The lower limit of the carbon star progenitor mass predicted by the Padova models is clearly incorrect from our IRS spectra if our estimated luminosity values are accurate. Unless 30%–50% of the PPN luminosity is not being detected, our observations do not agree with the dredge-up predictions of the Padova models. In the case of the two SMC objects in our sample the derived luminosities correspond to low progenitor masses according to the Padova models, and those models predict that these stars should not be carbon-rich. For the SMC metallicity the Padova models predict a minimum carbon star progenitor mass of 1.15 $M_{\odot}$, and a minimum tip of the AGB carbon star luminosity of about 6000 $L_{\odot}$. The observed luminosities of our two SMC objects are about 25% lower than this. Even allowing for the estimated uncertainties in the derived luminosity, neither object should be carbon-rich according to the Padova models. This suggests that the carbon dredge-up efficiency in the stars is somewhat better than what is assumed in the Padova models.

9. SUMMARY AND CONCLUSIONS

We have discovered a sample of 17 carbon-rich PPNe from various *Spitzer* spectroscopic programs observing objects in the LMC and the SMC. Fifteen of these objects are similar to the Galactic carbon-rich PPNe, while the remaining two objects have unusual spectra but still appear to be carbon-rich PPNe. Of the 15 "normal" carbon-rich PPNe, 7 have obvious 21 μm features, in 2 the feature is weak but clearly present, and for 4 other objects the feature is either very weak or questionable. The remaining 2 objects of the sample of 15 objects do not have the 21 μm feature. One of these two objects without the feature is a hot star, of spectral type B0.5I(e). The other object, J055831, may be a hot star based upon the similarity of its IRS spectrum to those of young [WC] PNe in the Galaxy, which is also the case for the SMC object J010546 with a questionable 21 μm detection. Object J055831 may have weak crystalline silicate features in its IRS spectrum, while J010546 does not show any sign of crystalline silicate features in the 22–30 μm wavelength range.

Four of the 15 objects appear to have the 11 μm SiC feature in their spectra along with the 11.2 μm UIR feature and its associated plateau to longer wavelengths. This has not been noted previously in the 21 μm sources, although looking back at the available *ISO* and *Spitzer* spectra of 21 μm objects it appears that one object, IRAS 22272+5435, also has a weak SiC feature in its spectrum.

The two additional objects in the sample have unusual mid-infrared spectra showing a very strong emission feature near 11 μm. This feature is tentatively attributed to SiC emission; however the feature has an unusual shape and is much stronger than the SiC features observed in carbon star spectra. It is not entirely clear what the evolutionary status of these two unusual objects is, although the SEDs imply that these are PPNe. The feature is similar to strong SiC features observed in a small number of PNe in the LMC (Bernard-Salas et al. 2009).

The general features of the dust emission from the objects showing the 21 μm feature appears to be similar to those of the Galactic 21 μm objects. Some differences in the detailed properties can be identified—the peak dust temperatures appear to be 80–120 K higher in these PPNe than for the Galactic 21 μm objects as determined from radiative transfer models; the UIR emission is generally stronger in these objects than in Galactic PPNe; and there is clearly more structure visible in the UIR emission of these objects as well. In general, the UIR emission in the Magellanic Cloud objects is more like the ISM emission than is the case for the Galactic 21 μm objects, possibly indicating that there is more processing of the PAH molecules as they are produced in these objects than is the case for the Galactic objects. Since two of these Magellanic Cloud objects are known to be of spectral type F, there is clearly not enough ultraviolet radiation from the star to excite the observed level of UIR emission. Assuming that the UIRs are due to PAH molecules, this requires that the excitation be due in large part to optical photons. This means that the PAHs are larger in these objects than in the general ISM, where ultraviolet radiation is needed for the UIR excitation. This is also true of the Galactic 21 μm sources, almost all of which have spectral types of F and G, although the strength of the UIR features is not as great as in the Magellanic Cloud objects.

The 30 μm feature carries less of the infrared energy in the Magellanic Cloud objects than is the case for the Galactic objects. A good part of this difference appears to be due to the lower dust temperatures in the Galactic objects, rather than being due to having intrinsically weaker 30 μm features in the LMC and SMC objects.

As the distances to the LMC and SMC are known and the SEDs of the objects are well sampled by existing observations, we have been able to estimate the luminosities of these PPNe. We find a unexpectedly large range of luminosity from 4660 to 12,500 $L_{\odot}$ in our 17 objects. There is a general trend for the less luminous objects to have lower dust optical depths, which is what is expected for objects with a range of initial masses leaving the AGB. However, the fraction of higher luminosity objects is surprisingly large and the lowest luminosity objects are found to be too faint to have become carbon stars on the AGB according to the stellar evolution models of Karakas et al. (2002). This is also a problem for some of the recent synthetic AGB model parameterizations for the LMC, such as Girardi & Marigo (2007). Only 6 of the 17 objects in our sample have estimated luminosities consistent with being carbon stars at the end of the AGB according to the Marigo and Girardi models.

There is some indication that the sky distribution of these PPNe differs from that of their expected progenitor objects, the extreme carbon stars and the general AGB M-type star and carbon star populations of the Clouds. We can demonstrate that PPN candidates selected as having photometric colors similar to our small sample of PPNe have sky distributions that are different from either the carbon stars or the very dusty objects in the LMC and the SMC. If these candidate objects are mostly PPNe as expected, then the total number of 21 μm objects in the Clouds will be much larger than the sample discussed in this paper.

This work is primarily based on observations made with the *Spitzer Space Telescope*, which is operated by the Jet Propulsion Laboratory, California Institute of Technology, under a contract with NASA. Support for this research was provided by NASA through contract 1378453 issued by JPL/Caltech. R.Sz. acknowledges support by grant N203 511838 from the Polish MNiSW.

This paper makes use of observations obtained at the Gemini Observatory, which is operated by the Association of Universities for Research in Astronomy, Inc., under a cooperative agreement with the NSF on behalf of the Gemini partnership: the National Science Foundation (United States), the Science and Technology Facilities Council (United Kingdom), the National Research Council (Canada), CONICYT (Chile), the Australian Research Council (Australia), Ministèrio da Ciência e Tecnologia (Brazil), and Ministerio de Ciencia, Tecnología e Innovación Productiva (Argentina).

This research has made use of the SIMBAD database, operated at CDS, Strasbourg, France, the NASA/IPAC Infrared Science Archive, which is operated by the Jet Propulsion Laboratory, California Institute of Technology, under contract with the National Aeronautics and Space Administration, and NASA's Astrophysics Data System.

Facilities: Gemini:South, *Spitzer* (IRS)

REFERENCES

Beichman, C. A., Neugebauer, G., Habing, H. J., Clegg, P. E., & Chester, Th. J. 1988, Infrared Astronomical Satellite (IRAS) Catalogs and Atlases: Explanatory Supplement (Washington, DC: GPO)
Bientema, D. A., et al. 1996, A&A, 315, L369
Bernard-Salas, J., Peeters, E., Sloan, G. C., Cami, J., Guiles, S., & Houck, J. R. 2006, ApJ, 652, 29
Bernard-Salas, J., Peeters, E., Sloan, G. C., Gutenkunst, S., Matsuura, M., Tielens, A. G. G. M., Zijlstra, A. A., & Houck, J. R. 2009, ApJ, 699, 1541
Blöcker, T. 1995, A&A, 299, 755
Blum, R., et al. 2006, AJ, 132, 2034
Buss, R. H., Cohen, M., Tielens, A. G. G. M., Werner, M., Bregman, J. D., Witteborn, F., Rank, D., & Sandford, S. A. 1990, ApJ, 365, 23
Catalan, S., Isern, J., Garcia-Berro, E., & Ribas, I. 2008, MNRAS, 387, 1693
Cerrigone, L., Hora, J. L., Umana, G., & Trigilio, C. 2009, ApJ, 703, 585
Clayton, G. C. 1996, PASP, 108, 225
Clayton, G. C., et al. 2007, BAAS, 39, 890
Cohen, M., Barlow, M. J., Lie, X.-W., & Jones, A. F. 2002, MNRAS, 332, 879
Djorgovski, S. G., et al. 1999, in Wide Field Surveys in Cosmology, ed. S. Colombi, Y. Mellier, & B. Raban (Gif sur Yvette: Editions Frontieres), 89
Egan, M. P., et al. 2003, Air Force Research Laboratory Technical Report AFRL-VS-TR-2003-1589, ADA418993
Fazio, G. G., et al. 2004, ApJS, 154, 10
Fouqué, P., et al. 2000, A&AS, 141, 313
Girardi, L., & Marigo, P. 2007, A&A, 462, 237
Gordon, K. D. SAGE-SMC Legacy Team 2010, BAAS, 215, 459.21
Gruendl, R. A., Chu, Y.-H., Seale, J. P., Matsuura, M., Speck, A. K., Sloan, G. C., & Looney, L. W. 2008, ApJ, 688, L9
Higdon, S. J. U., et al. 2004, PASP, 116, 975
Hony, S., Waters, L. B. F. M., & Tielens, A. G. G. M. 2001, A&A, 378, 401
Hony, S., Waters, L. B. F. M., & Tielens, A. G. G. M. 2002, A&A, 390, 533
Houck, J. R., et al. 2004, ApJS, 154, 18
Hrivnak, B. J., Geballe, T. R., & Kwok, S. 2007, ApJ, 662, 1059
Hrivnak, B. J., Volk, K., Geballe, T. R., & Kwok, S. 2008, in IAU Symp. 251, Organic Matter in Space, ed. S. Kwok & S. A. Sanford (Cambridge: Cambridge Univ. Press), 213
Hrivnak, B. J., Volk, K., & Kwok, S. 2000, ApJ, 535, 275
Hrivnak, B. J., Volk, K., & Kwok, S. 2009, ApJ, 694, 1147
Izzard, R. G., Tout, C. A., Karakas, A. I., & Pols, O. R. 2004, MNRAS, 350, 407
Justtanont, K., Barlow, M. J., Skinner, C. J., Roche, P. F., & Smith, C. H. 1996, A&A, 309, 612
Karakas, A. I., Lattanzio, J. C., & Pols, O. R. 2002, PASA, 19, 515
Kemper, F., et al. 2010, PASP, 122, 683
Kessler, M., et al. 2003, The ISO Handbook, Vol. 1 (ESA SP-1262; Noordwijk: ESA)
Kraemer, K. E., Sloan, G. C., Price, S. D., Egan, M. P., & Wood, P. R. 2006, ApJ, 652, L25
Kurucz, R. L. 1993, Kurucz CD-Rom No. 13 (Cambridge, MA: SAO)
Kwok, S. 1993, ARA&A, 31, 63
Kwok, S., Volk, K., & Hrivnak, B. J. 1989, ApJ, 345, L51
Kwok, S., Volk, K., & Hrivnak, B. J. 2002, ApJ, 573, 720
Lasker, B. M., et al. 2008, AJ, 136, 735
Le Bertre, T., Lebre, A., & Waelkens, C. (ed.) 1999, IAU Symp. 191, Asymptotic Giant Branch Stars (San Francisco, CA: ASP)
Lebouteiller, V., Bernard-Salas, J., Sloan, G. C., & Barry, D. J. 2010, PASP, 122, 231
Leisy, P., Dennefeld, M., Alard, C., & Guibert, J. 1997, A&AS, 121, 407
Leung, C. M. 1976, ApJ, 209, 75
Marigo, P., & Girardi, L. 2007, A&A, 469, 239
Marshall, J. R., van Loon, J. Th., Matsuura, M., Wood, P. R., Zijlstra, A. A., & Whitelock, P. A. 2004, MNRAS, 355, 1348
Matsuura, M., et al. 2009, MNRAS, 396, 918
McNamara, D. H., Clementini, G., & Marconi, M. 2007, AJ, 133, 2752
Meixner, M., et al. 2006, AJ, 132, 2268
Mill, J. D., et al. 1994, J. Spacecr. Rockets, 31, 900
Monet, D. G., et al. 2003, AJ, 125, 984
Mucciarelli, A., Ferraro, F. R., Origlia, L., & Pecci, F. F. 2007, AJ, 133, 2053
Neugebauer, G., et al. 1984, ApJ, 278, 1
Olnon, F. M., et al. 1986, A&AS, 65, 607
Peeters, E., Hony, S., van Kerchhoven, C., Tielens, A. G. G. M., Allamandola, L. J., Hudgins, D. M., & Bauschlicher, C. W. 2002, A&A, 390, 1089
Pegourie, R. 1988, A&A, 194, 335
Pei, A., & Volk, K. 2003, in IAU Symp. 209, Planetary Nebulae: Their Evolution and Role in the Universe, ed. S. Kwok, M. Dopita, & R. Sutherland (San Francisco, CA: ASP), 305
Posch, Th., Mutschke, H., & Anderson, A. 2004, ApJ, 616, 1167
Raman, V. V., & Anandarao, B. G. 2008, MNRAS, 385, 1076
Reid, N., Tinney, C., & Mould, J. 1990, ApJ, 348, 98
Rieke, G. H., et al. 2004, ApJS, 154, 1
Rouleau, F., & Martin, P. G. 1991, ApJ, 377, 526

Schönberner, D. 1979, A&A, 79, 108
Skrutskie, M. F., et al. 2006, AJ, 131, 1163
Speck, A. K., & Barlow, M. J. 1997, Ap&SS, 251, 115
Storm, J., Carney, B. W., Geiren, W. P., Fouque, P., Latham, D. W., & Fry, A. M. 2004, A&A, 415, 531
Su, K. Y. L., Volk, K., Kwok, S., & Hrivnak, B. J. 1998, ApJ, 508, 744
Szczerba, R., & Górny, S. K. (ed.) 2001, Post-AGB Objects as a Phase of Stellar Evolution (Astrophysics and Space Science Library, Vol. 265; Dordrecht: Kluwer)
Szczerba, R., Siódmiak, N., Stasińska, G., & Borkowski, J. 2007, A&A, 469, 799
Tielens, A. G. G. M. 2008, ARA&A, 46, 289
Trams, N. R., et al. 1999, A&A, 346, 843
van Aarle, E., van Winckel, H., Evan, T. L., & Wood, P. 2011, A&A, in press
van Diedenhoven, B., Peeters, E., Van Kerchhoven, C., Hony, S., Hudgins, D. M., Allamandolla, L. J., & Tielens, A. G. G. M. 2004, ApJ, 611, 928
van Loon, J. Th., Marshall, J. R., & Zijlstra, A. A. 2005, A&A, 442, 597
van Loon, J. Th., Zijlstra, A. A., Whitelock, P. A., Waters, L. B. F. M., Loup, C., & Trams, N. R. 1997, A&A, 325, 585
van Winckel, H. 2003, ARA&A, 41, 391
Volk, K., Kwok, S., & Hrivnak, B. J. 1999, ApJ, 516, 99
Volk, K., Kwok, S., Hrivnak, B. J., & Szczerba, R. 2002, ApJ, 567, 412
Volk, K., Xiong, G.-Z., & Kwok, S. 2000, ApJ, 503, 408
Werner, M., et al. 2004, ApJS, 154, 1
Will, J. M., et al. 1995, A&AS, 112, 367
Woods, P. M., et al. 2011, MNRAS, 411, 1597
Zaritsky, D., Harris, J., & Thompson, I. 1997, AJ, 114, 1002
Zhang, K., Jiang, B. W., & Li, A. 2009, ApJ, 702, 680
Zhang, Y., Kwok, S., & Hrivnak, B. J. 2010, ApJ, 725, 990
Zijlstra, A. A., Gaylard, M. J., te Lintel Hekkert, P., Menzias, J., Nyman, L.-A., & Schwarz, H. E. 1991, A&A, 243, 9